

A Comparison of Stratospheric Gravity Waves in a High-Resolution General Circulation Model with 3-D Satellite Observations

Haruka Okui¹, Corwin James Wright², Neil P Hindley², Emily J Lear², and Kaoru Sato¹

¹The University of Tokyo

²University of Bath

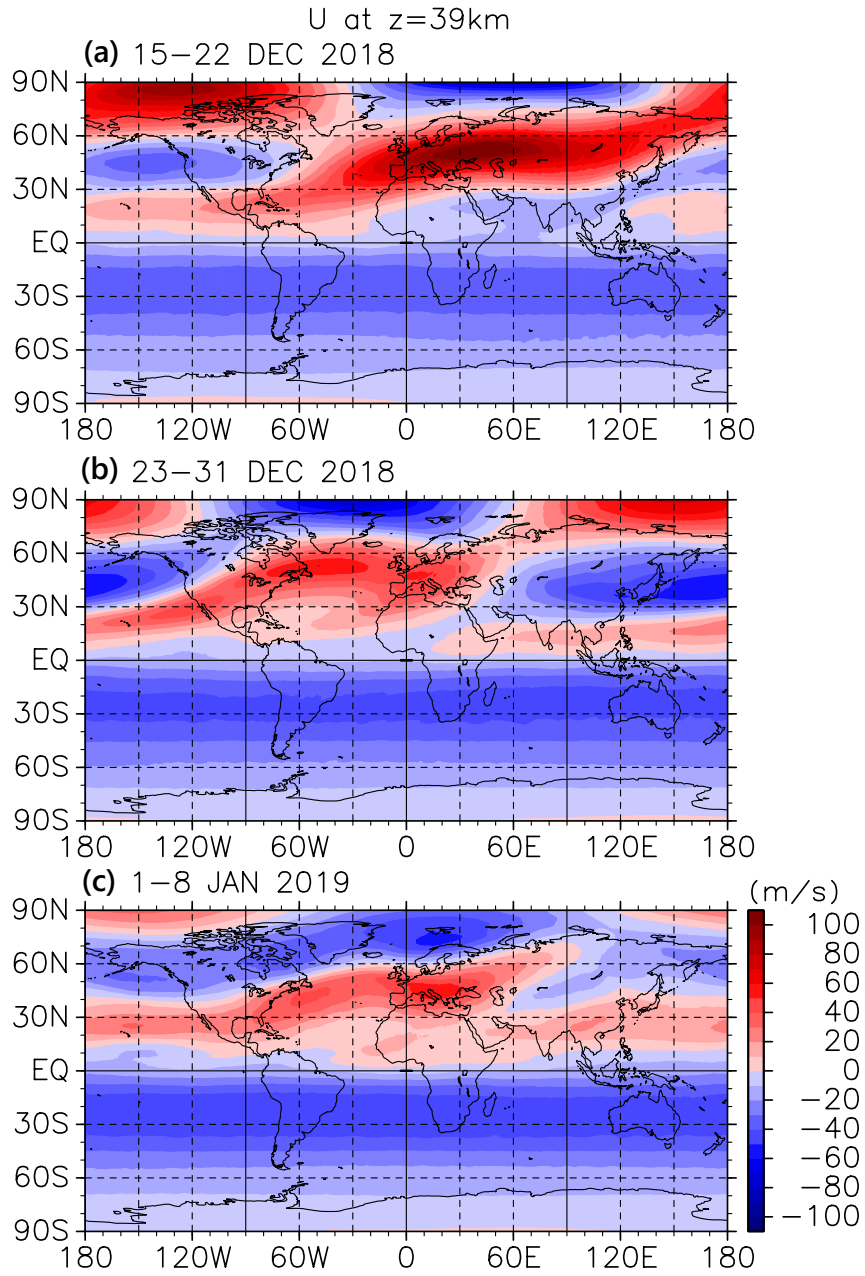
March 9, 2023

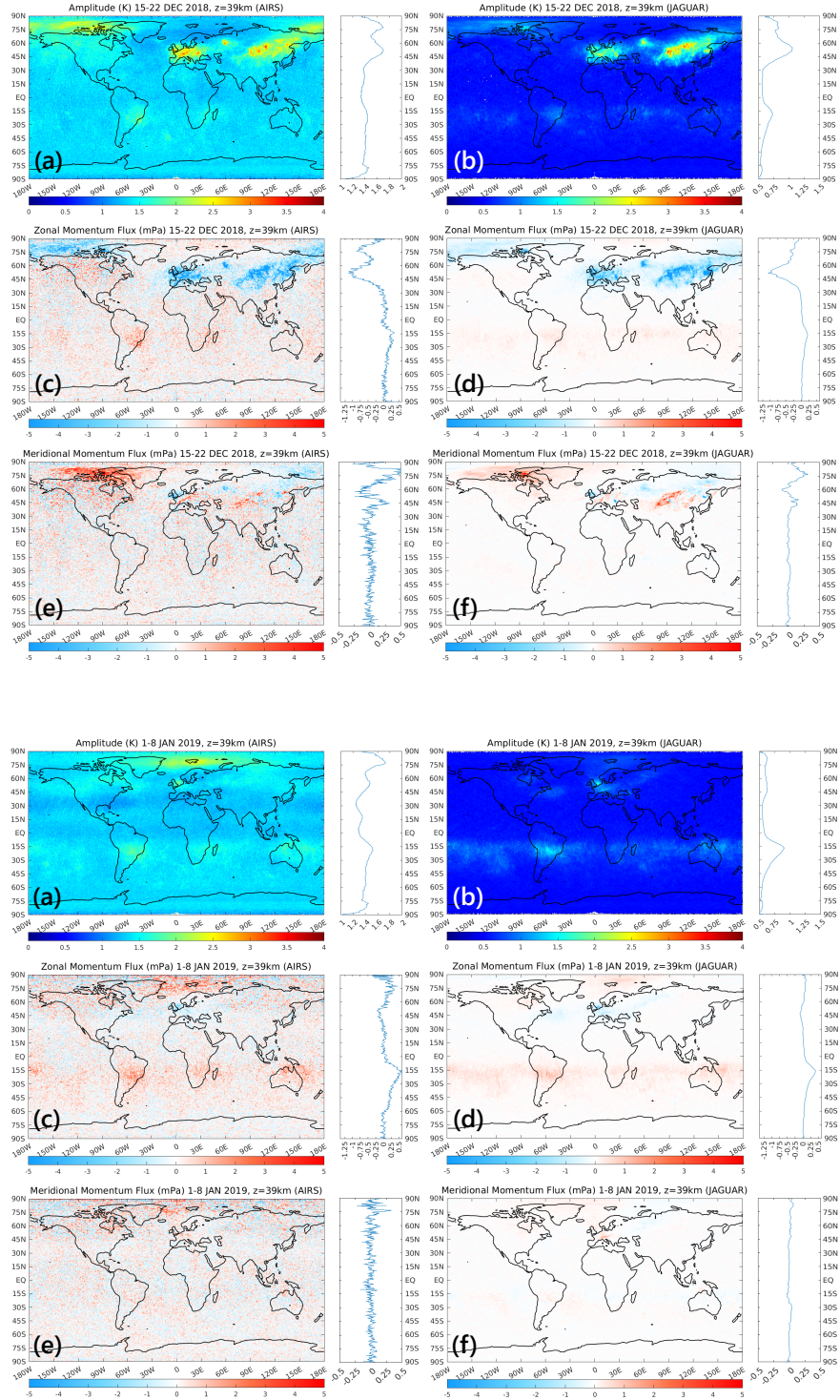
Abstract

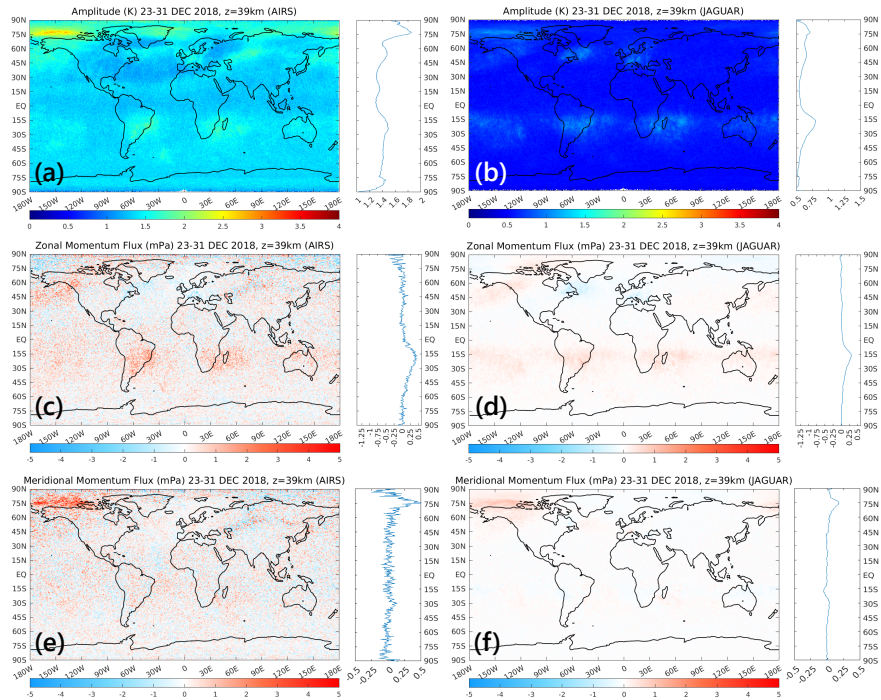
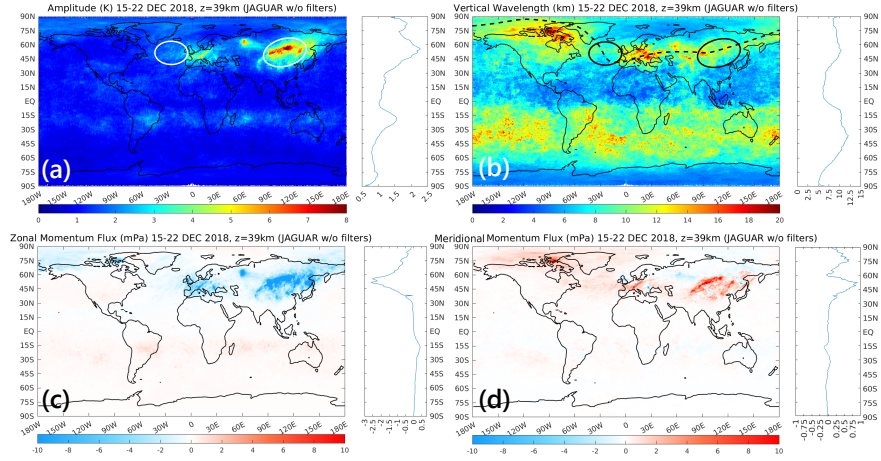
Atmospheric gravity waves (GWs) play a key role in determining the thermodynamical structure of the Earth's middle atmosphere. Despite the small spatial and temporal scales of these waves, a few high-top general circulation models (GCMs) that can resolve them explicitly have recently become available. This study compares global GW characteristics simulated in one such GCM, the Japanese Atmospheric GCM for Upper-Atmosphere Research (JAGUAR), with those derived from three-dimensional (3-D) temperatures observed by the Atmospheric Infrared Sounder (AIRS) aboard NASA's Aqua satellite. The target period is from 15 December 2018 to 8 January 2019, including the onset of a major sudden stratospheric warming (SSW). The 3-D Stockwell transform method is used for GW spectral analysis. The amplitudes and momentum fluxes of GWs in JAGUAR are generally in good quantitative agreement with those in the AIRS observations in both magnitude and distribution. As the SSW event progressed, the GW amplitudes and eastward momentum flux increased at low latitudes in the summer hemisphere in both the model and observation datasets. Case studies demonstrate that the model is able to reproduce comparable wave events to those in the AIRS observations with some differences, especially noticeable at low latitudes in the summer hemisphere. Through a comparison between the model results with and without the AIRS observational filter applied, it is suggested that the amplitudes of GWs near the exits and entrances of eastward jet streaks are underestimated in AIRS observations.

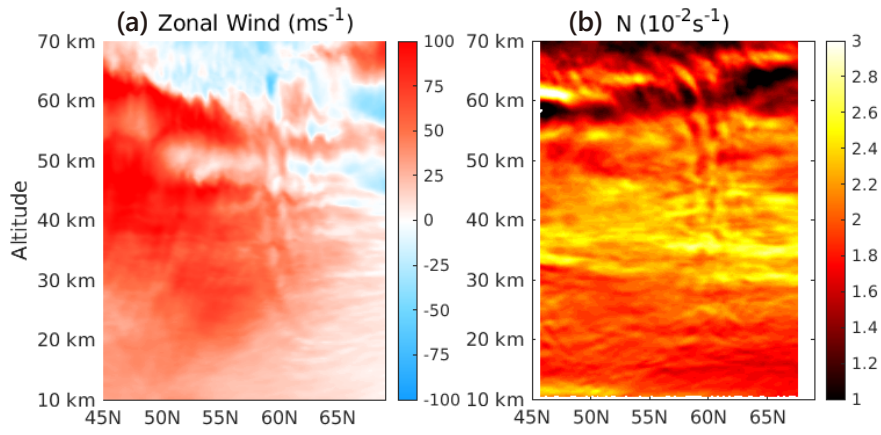
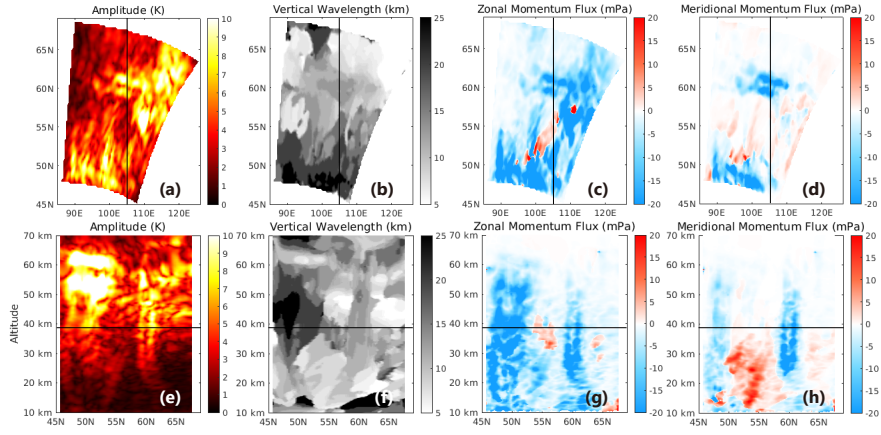
Hosted file

957426_0_art_file_10758090_rqv4x8.docx available at <https://authorea.com/users/558845/articles/627587-a-comparison-of-stratospheric-gravity-waves-in-a-high-resolution-general-circulation-model-with-3-d-satellite-observations>

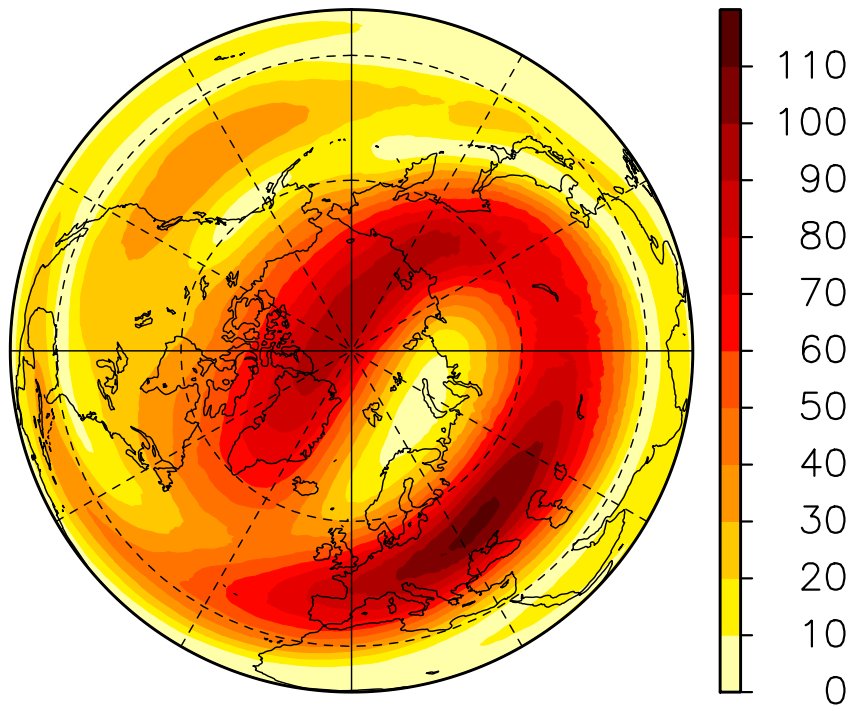


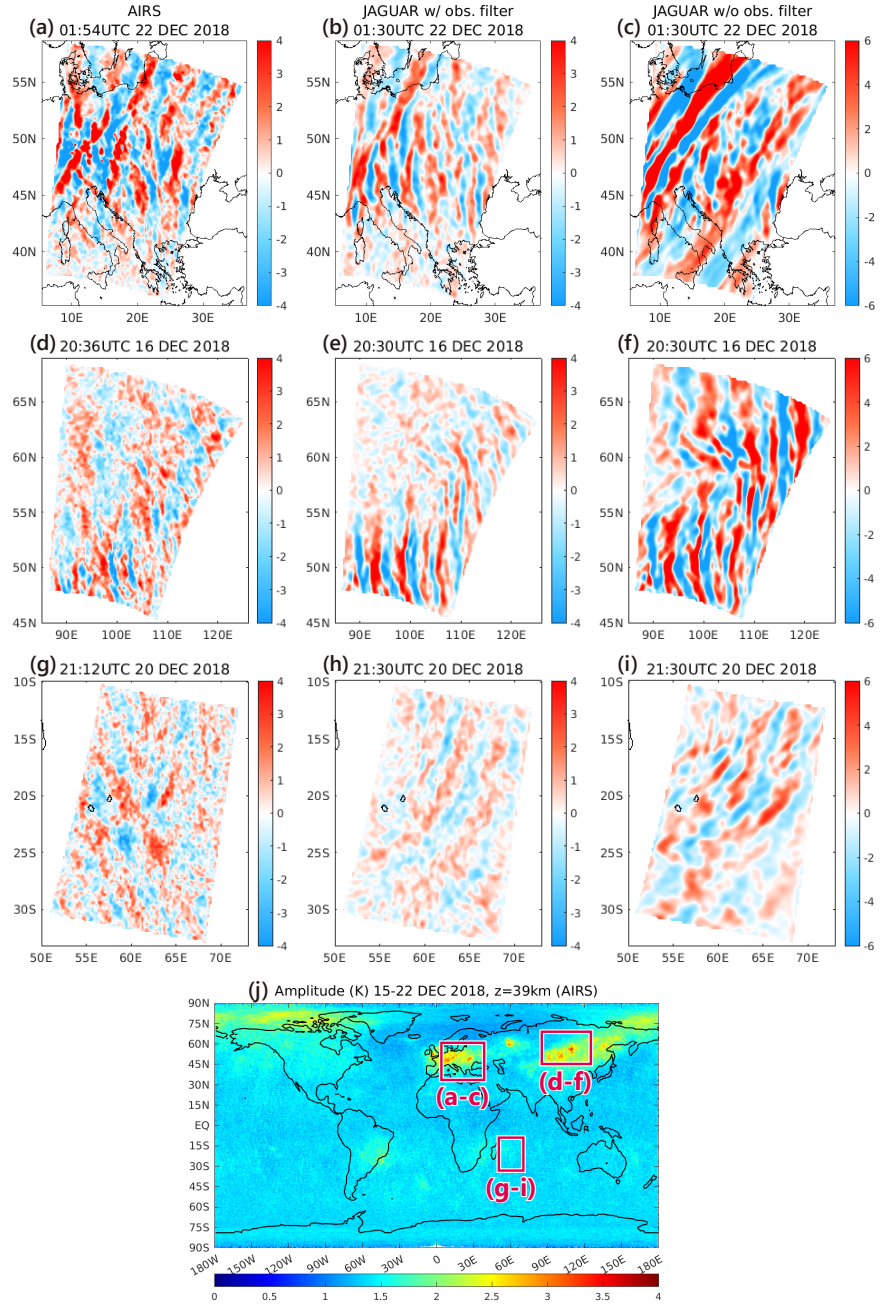






$|u|$ at $z=39\text{km}$
15–22 DEC 2018





1
2 **A Comparison of Stratospheric Gravity Waves in a High-Resolution General**
3 **Circulation Model with 3-D Satellite Observations**

4
5 **H. Okui¹, C. J. Wright², N. P. Hindley², E. J. Lear², and K. Sato¹**

6
7 ¹ Department of Earth and Planetary Science, The University of Tokyo, Tokyo, Japan.

8 ² Centre for Space, Atmospheric and Oceanic Science, University of Bath, Bath, UK.

9
10 Corresponding author: Haruka Okui (okui@eps.s.u-tokyo.ac.jp)

11
12 **Key Points:**

- 13
- 14 • Stratospheric gravity waves (GWs) in a GW-permitting high-top general circulation model are validated globally for a boreal winter
 - 15 • The global characteristics of GWs and their variation during a sudden stratospheric warming are explored using the 3-D Stockwell transform
 - 16 • Better model representation of convection and higher vertical resolution of the nadir-viewing instrument could provide better GW coverage
- 17
18
19

20 **Abstract**

21 Atmospheric gravity waves (GWs) play a key role in determining the thermodynamical structure
22 of the Earth's middle atmosphere. Despite the small spatial and temporal scales of these waves, a
23 few high-top general circulation models (GCMs) that can resolve them explicitly have recently
24 become available. This study compares global GW characteristics simulated in one such GCM,
25 the Japanese Atmospheric GCM for Upper-Atmosphere Research (JAGUAR), with those
26 derived from three-dimensional (3-D) temperatures observed by the Atmospheric Infrared
27 Sounder (AIRS) aboard NASA's Aqua satellite. The target period is from 15 December 2018 to
28 8 January 2019, including the onset of a major sudden stratospheric warming (SSW). The 3-D
29 Stockwell transform method is used for GW spectral analysis. The amplitudes and momentum
30 fluxes of GWs in JAGUAR are generally in good quantitative agreement with those in the AIRS
31 observations in both magnitude and distribution. As the SSW event progressed, the GW
32 amplitudes and eastward momentum flux increased at low latitudes in the summer hemisphere in
33 both the model and observation datasets. Case studies demonstrate that the model is able to
34 reproduce comparable wave events to those in the AIRS observations with some differences,
35 especially noticeable at low latitudes in the summer hemisphere. Through a comparison between
36 the model results with and without the AIRS observational filter applied, it is suggested that the
37 amplitudes of GWs near the entrance or exit of an eastward jet streak are underestimated in
38 AIRS observations.

39 **Plain Language Summary**

40 Atmospheric gravity waves play key roles in the dynamics of the stratosphere, mesosphere and
41 thermosphere. Three-dimensional satellite observations and high-resolution general circulation
42 models are of broad use to further our understanding of their global characteristics. This is the
43 first study to make a quantitative comparison of the global distribution of the amplitudes and
44 momentum fluxes of gravity waves in the gravity-wave-permitting high-top general circulation
45 model (GCM), Japanese Atmospheric GCM for Upper-Atmosphere Research (JAGUAR), with
46 those derived from three-dimensional temperature measurements by Atmospheric Infrared
47 Sounder (AIRS) on NASA's Aqua satellite. Good agreement in both magnitude and distribution
48 of gravity wave activity is demonstrated between the JAGUAR and AIRS temperatures. There
49 are relatively large differences in tropical regions in the summer hemisphere, where convective
50 gravity waves are expected to be dominant. Comparison of model-simulated gravity waves with
51 and without the AIRS vertical resolution applied indicates that gravity waves near the entrance or
52 exit of an eastward jet streak may be overlooked in AIRS observations.

53 **1 Introduction**

54 Atmospheric gravity waves (GWs) are of crucial importance for the dynamics of the
55 Earth's middle atmosphere. Transporting energy and momentum, these waves play an essential
56 role in driving the temperatures and circulations in the middle atmosphere away from the
57 radiative equilibrium state. A major portion of the GW momentum flux is carried by waves
58 generated in the lower atmosphere. Their sources include topography, jets and fronts, convection,
59 and strong wind shear. They propagate upward and deposit momentum into the atmospheric
60 layer where they break or dissipate. This momentum deposition, or GW forcing, is the main
61 driver of the mesospheric circulation (e.g., Andrews et al., 1987). It also drives or modulates
62 phenomena in the stratosphere, such as the quasi-biennial oscillation (e.g., Baldwin et al., 2001;
63 Dunkerton, 1997; Sato & Dunkerton, 1997).

64 In recent years, there has been growing interest in the contribution of GWs to the onset of
65 stratospheric sudden warmings (SSWs) and the whole atmospheric response to SSWs. Although
66 SSWs themselves are caused by strong planetary wave forcing, several studies showed that not
67 only planetary waves but also GWs contribute to the occurrence of vortex preconditioning for
68 SSWs (e.g., Albers & Birner, 2014; Wright et al., 2010). SSWs also have a notable impact on the
69 mesosphere. An elevated stratopause is a jump of the stratopause to an upper mesospheric height
70 several days after an SSW (Manney et al., 2008, 2009). It has been shown that both planetary
71 waves and GWs are responsible for the formation and/or descent of elevated stratopause events
72 (e.g., Chandran et al., 2011, 2013; Limpasuvan et al., 2012, 2016; Okui et al., 2021; Siskind et
73 al., 2010; Thurairajah et al., 2014; Tomikawa et al., 2012). In addition to the phenomena in the
74 winter hemisphere as mentioned above, the roles of GWs in the modification of the global
75 middle atmosphere associated with SSWs has received considerable attention: Interhemispheric
76 coupling is a lag correlation between the dynamical activity in the winter polar stratosphere, as
77 typified by SSWs, and the temperatures in the polar upper mesosphere in the summer
78 hemisphere. Though the mechanism is not yet fully understood, it is widely accepted that GWs
79 are one of the key factors in this phenomenon (Körnich & Becker, 2010; Smith et al., 2020;
80 Yasui et al., 2021). As such, careful quantitative evaluation of GW activity before and after
81 SSWs will help enhance our understanding of the dynamical mechanisms of these phenomena.

82 To understand global characteristics of GWs, high-resolution satellite observations are a
83 key tool. Ern et al. (2018) produced a global climatology of GW parameters using two satellite
84 infrared limb sounders: High Resolution Dynamics Limb Sounder (HIRDLS) and Sounding of
85 the Atmosphere using Broadband Emission Radiometry (SABER). These limb sounders have
86 quite high vertical resolutions, namely 1 km for HIRDLS and 2 km for SABER (e.g., Barnett et
87 al., 2008; Gille et al., 2003, 2008; Wright et al., 2011). However, their horizontal resolutions are
88 much poorer (several hundreds of kilometers) and only horizontal wavelengths along the line of
89 sight of the instruments can be obtained. Thus, the horizontal wavelengths and, hence,
90 momentum fluxes of GWs are very likely to be overestimated.

91 To fully comprehend GW structure, three-dimensional (3-D) observations and 3-D
92 analysis methods are necessary. In contrast to limb sounding, nadir-viewing satellite instruments,
93 such as the Atmospheric Infrared Sounder (AIRS) on NASA's Aqua satellite, are characterized
94 by high horizontal resolutions and low vertical resolutions. One approach to consistently observe
95 3-D GW structure is combining limb- and nadir-sounding instruments (Alexander & Teitelbaum,
96 2011; Wright et al., 2016a, 2016b). In addition, the recent development of 3-D spectral analysis
97 techniques (Ern et al., 2017; Hindley et al., 2019; Wright et al., 2017, 2021) has made global 3-D
98 GW measurements possible using the 3-D temperature retrieval for AIRS (Hoffmann &
99 Alexander 2009).

100 Evaluation of the impact of observational filters on GW characteristics is also needed.
101 Observational filters are limitations in observable spectral range depending on instruments and
102 observational techniques. These filters for satellite instruments are determined by the sensitivity
103 and sampling geometry. In this sense, intercomparison of satellite observations is worthwhile.
104 Wright et al. (2011) compared the Constellation Observing System for Meteorology Ionosphere
105 and Climate (COSMIC), HIRDLS and SABER. Similarly, Meyer et al. (2018) made a global
106 comparison between AIRS and HIRDLS. These two studies showed that these instruments
107 basically give close agreement in the relative distribution of large amplitudes but those having
108 coarser vertical resolutions fail to obtain significant parts of a GW spectrum.

109 Recently, GW-permitting high-top GCMs have become available. As an example of this,
110 Watanabe et al. (2022) visualized 3-D structure and propagation of GWs in a T639L340 whole
111 neutral atmosphere GCM called the Japanese Atmospheric GCM for Upper Atmosphere
112 Research (JAGUAR, Watanabe & Miyahara, 2009). JAGUAR is capable of reproducing the
113 universal spectrum (e.g., VanZandt, 1985; Tsuda et al., 1989; Sato et al., 2003), which is
114 characterized by a steep slope of vertical wavenumber (m) spectra ($\propto \sim m^{-3}$) at high
115 wavenumbers of $m = \sim 10^{-4} - 10^{-3} \text{ m}^{-1}$ (Okui et al., 2022). Kruse et al. (2022), meanwhile
116 demonstrated extremely good skill for four state-of-the-art numerical weather prediction models
117 at reproducing AIRS-observed orographic waves around the Drake Passage. While two of the
118 four models in this study were local-area in nature, two others, namely the Integrated Forecast
119 System (IFS) and the Icosahedral Nonhydrostatic (ICON) model, were run globally with vertical
120 domains from the surface up to ~ 80 km. Finally, Vadas and Becker (2018) and Becker and
121 Vadas (2018) demonstrated secondary generation of GWs caused by primary orographic GWs
122 using the Kühlungsborn Mechanistic general Circulation Model (KMCM; Becker, 2009). Becker
123 and Vadas (2020) later extended the height range of this model to ~ 450 km, renaming it to the
124 High Altitude Mechanistic general Circulation Model (HIAMCM). Using this model, Becker et
125 al. (2022) nudged the troposphere, stratosphere and lower mesosphere of HIAMCM to
126 reanalysis. They demonstrated that the model simulated a GW event over Northern Europe in
127 January 2016 consistently with AIRS temperature measurements. However, although such
128 GCMs can resolve a major part of GWs in the middle atmosphere, due to resolution limitations
129 even in the perfect case it is still impossible for them to cover the whole spectral range of GWs.

130 Since no observations or model simulations can provide full information on the global
131 characteristics of GWs, GW distributions and behavior should be carefully examined by
132 intercomparing different models and instruments. Accordingly, Geller et al. (2013) compared
133 absolute GW momentum fluxes in a 85-km-top high-resolution model, the Kanto model
134 (Watanabe et al., 2008), with those derived from SABER and HIRDLS observations. The Kanto
135 model, the predecessor of the JAGUAR model, and a low-top high-resolution model,
136 Community Atmosphere Model, version 5 (CAM5) in general agreed better with the
137 observations than other climate models did. Regarding the state-of-the-art GW-permitting high-
138 top GCMs mentioned above, validation of model-simulated GWs using observations is mostly
139 limited to local comparisons (Becker et al., 2022; Kruse et al., 2022). The global distribution of
140 GW momentum flux, combined with careful GW validation and examination of the spectral
141 coverage, will also be informative for improvement of GW parameterization schemes.

142 In this study, we compare global GW characteristics between hindcast simulations
143 performed with JAGUAR and 3-D AIRS observations. In doing so, we validate the GWs in
144 JAGUAR against AIRS and, in addition, are able to estimate the possible impact of the coarse
145 vertical resolution of AIRS on observed GWs by comparing two datasets from JAGUAR with
146 and without a vertical low-pass filter acting as an analogue of AIRS' resolution limitations. In
147 this paper, we show results from December 2018 to January 2019. This period contains an SSW
148 whose onset occurred on 1 January 2019. Thus, variability in GW activity during the SSW event
149 is also described.

150 This paper begins by describing details of the observations and model simulation and
151 explaining the 3-D Stockwell (S-) transform, which we used for GW spectral analysis. Section 3
152 first addresses comparisons of global distribution of GW amplitude and momentum flux and
153 their variability before and after the 2019 SSW. Then, we take a closer look at some GW events.

154 Section 4 discusses the mechanisms of the distribution of GW characteristics described in the
155 previous section, the effect of an SSW on GW activity, and possible reasons for the agreement
156 and disagreement found in the AIRS and JAGUAR results. We summarize and provide some
157 concluding remarks in Section 5.
158

159 **2 Data and Methods**

160 **2.1 AIRS**

161 AIRS is a nadir-sounding satellite instrument on NASA's Aqua satellite (Aumann et al.,
162 2003; Chahine et al., 2006). The satellite flies in a sun-synchronous near-polar orbit, completing
163 14.55 orbits per day. Viewing in the nadir of the satellite, AIRS has a good ability to observe fine
164 horizontal-scale structures. The instrument scans a continuous 1780 km-wide swath of 90 pixels
165 with a horizontal resolution varying from $\sim 13.5 \text{ km} \times 13.5 \text{ km}$ at nadir to $\sim 41 \text{ km} \times 21.4 \text{ km}$ at
166 track edge. The data are sectioned into 135-pixel along-track pieces, referred to as granules,
167 whose lengths are roughly 2250 km. There are 240 granules per day, corresponding to 6 minutes
168 of data collection each. AIRS has 2378 spectral channels. We analyze 3-D temperatures derived
169 from AIRS infrared radiance measurements in the 4.3 and 15 μm infrared CO₂ channels,
170 retrieved using the method described by Hoffmann and Alexander (2009). The vertical resolution
171 of the retrieved temperature is 7–20 km over an altitude range of $z = 15\text{--}60 \text{ km}$ (Hindley et al.,
172 2019). The assumption of local thermodynamic equilibrium, used in the retrieval scheme, is
173 violated during daytime and, to reduce this influence, the daytime retrieval only uses the 15 μm
174 channel. As a result, the vertical resolution is coarser for the daytime retrieval (see Fig. 2b of
175 Hindley et al., 2019). To examine a sufficient number of granules even at summer latitudes, we
176 analyzed the global characteristics using both daytime and nighttime observations. In case
177 studies presented in Section 3.3, only the results from nighttime observations are shown.

178 **2.2 JAGUAR**

179 Temperature perturbations in hindcast simulations performed with a GW-permitting
180 GCM, JAGUAR, are compared with those in AIRS observations. JAGUAR is a hydrostatic
181 global spectral model using a T639 triangular truncation, which is capable of resolving
182 horizontal wavelengths longer than $\sim 60 \text{ km}$ (Watanabe & Miyahara, 2009). The model contains
183 340 vertical layers from the surface to the lower thermosphere ($\sim 150 \text{ km}$) with a constant log-
184 pressure height interval of 300 m. No parameterization schemes for sub-grid-scale GWs are
185 applied in this model. Cumulus convection is parameterized by using the scheme presented by
186 Arakawa and Schubert (1974).

187 Hindcast simulations using JAGUAR were performed for boreal winter 2018–2019. The
188 model was initialized by 3-day spectral nudging to a reanalysis dataset created by the JAGUAR-
189 Data Assimilation System (JAGUAR-DAS; Koshin et al., 2020, 2022). This nudging process
190 relaxes only the low total horizontal wavenumber (n) components of $n = 0\text{--}15$ to the reanalysis
191 data, leaving GWs and other high n components ($n \geq 16$) free to evolve. Supporting this, the
192 ERA5 reanalysis dataset (Hersbach et al., 2020) was used to constrain $n = 0\text{--}15$ in the
193 troposphere ($> 200 \text{ hPa}$), where the reliability of the JAGUAR-DAS reanalysis is relatively low
194 compared to ERA5. After the initializations, a series of 4-day free-run simulations were
195 performed. These free-runs from December 2018 to 8 January 2019 with a 4-day interval are
196 analyzed in this study. The period contains an Arctic major SSW occurring around New Year's

197 Day in 2019 (Rao et al., 2019). The background wind field during this period, which can affect
198 the generation, propagation and attenuation of GWs, significantly changed as a result of this
199 event, and thus the averages shown in this study are taken individually over the separate periods
200 of 15–22, 23–31 December 2018 and 1–8 January 2019, which correspond to a period with the
201 stable stratospheric winter jet, and the periods before and after an SSW, respectively.

202 To provide a fair comparison with AIRS temperature perturbations, the temperature
203 output from JAGUAR simulations was resampled as the AIRS footprints by using linear
204 interpolation. Hindley et al. (2021), who compared GWs in a local-area configuration of the UK
205 Met Office Unified Model (1.5 km grid, 118 vertical levels) with AIRS, first convolved the
206 model-simulated temperature field with a horizontal Gaussian function with a full width at half
207 maximum (FWHM) of 13.5 km×13.5 km and then resampled the model data as the AIRS
208 footprints. In this study, such horizontal filters were not applied because there is no considerable
209 difference in horizontal resolutions between JAGUAR and AIRS. Since the JAGUAR outputs
210 were averaged to a 1-hour frequency, this resampling was performed on the JAGUAR data
211 whose representative time (the central time of the averaged time period) is closest to the
212 observation time of each AIRS granule. For example, Granule 127 on 16 December 2018, which
213 corresponds to the AIRS observation from 13:42UTC to 13:48UTC on 16 December 2018, was
214 compared with JAGUAR data at 13:30UTC on the same day.

215 The vertical resolution of the 3-D AIRS temperature retrieval was also applied to the
216 JAGUAR temperatures. Before doing that, we extracted one model layer every three (i.e., at a
217 constant log-pressure height interval of 900 m) to reduce computational cost. Since the vertical
218 resolution of AIRS is coarser by an order of magnitude than 900 m, it is expected that the
219 influence of this extraction on the results is limited. Then, the extracted model layers were
220 linearly interpolated onto a regular geopotential height grid from the surface to $z=90$ km in 1 km
221 steps. We then used the method of the AIRS vertical resolution application described in Hindley
222 et al. (2021). This involved calculating the convolution of the model temperature profiles using
223 vertical Gaussian functions with FWHMs corresponding to the AIRS vertical resolution (see Fig.
224 2b of Hindley et al., 2019) for each altitude. Finally, we added noise to the model data to
225 simulate the AIRS retrieval noise following the method described by Hindley et al. (2019). The
226 residual perturbations (refer to Section 2.3 for the definition) in Granule 1 at 00:00 UTC on 15
227 December 2018, which contains no discernible waves, are horizontally randomized and added to
228 the resampled JAGUAR granules.

229 To discuss the effect of the observational filter and retrieval noise, the results for
230 JAGUAR without the applications of the AIRS vertical resolution and retrieval noise are also
231 shown in Section 3. The model layers were interpolated onto a 300-m geopotential height grid
232 for the preparation of these data. They are hereafter referred to as JAGUAR without the
233 observational filter. On the other hand, JAGUAR with the observational filter denotes the model
234 data with all the process described above applied. In addition to wave features, horizontal winds
235 in JAGUAR are described in the following sections. Note that the altitudes on all the figures
236 from JAGUAR are not the log-pressure height but the geopotential height.

237 2.3 The 3-D S-Transform

238 The N-dimensional S-transform (Stockwell et al., 1996) application developed by
239 Hindley et al. (2019) was used here for spectral analysis of 3-D temperature perturbations. First,
240 the method of GW extraction is as follows: AIRS temperatures and JAGUAR temperatures

241 resampled as AIRS footprints are interpolated onto a regular horizontal grid with a constant
 242 interval of 20 km. Fitting fourth-order polynomials in the cross-track direction, the background
 243 temperatures (\bar{T}) are extracted from the original temperature fields, following the method
 244 described in Alexander and Barnett (2007). The residual perturbations T' , containing GWs and
 245 noise, are used for the spectral analysis. The resulting temperature perturbations are sensitive to
 246 waves having vertical wavelengths of $8 \lesssim \lambda_z \lesssim 40$ km and horizontal wavelengths λ_H from several
 247 tens of kilometres, depending on the angle from nadir, to $\lambda_H \sim 1000$ km (Ern et al., 2017;
 248 Hindley et al., 2019; Hoffmann et al., 2014).

249 Second, the 3-D S-transform was performed. To exclude pixel-to-pixel variations, waves
 250 with shorter λ_z than a threshold vertical wavelength λ_c or shorter λ_H than 60 km were ignored.
 251 The threshold was set as $\lambda_c = 6$ km for AIRS, 2 km for JAGUAR with the observational filter,
 252 and 1 km for JAGUAR without the observational filter. Only the dominant 1000 sets of
 253 wavenumbers in each granule are analyzed. The resulting 3-D S-transform object for each
 254 granule contains six-dimensional wave properties. To reduce the number of dimensions and
 255 computational expense, we only use the 3-D spatial structure of the properties of the dominant
 256 waves for each granule.

257 Rotating along- and cross-track wavenumbers by using the azimuth of the along-track
 258 direction at each grid, wave amplitude $|T'|$ and zonal, meridional and vertical wavenumbers
 259 (k, l, m) are finally obtained. Under the midfrequency assumption, namely $f \ll \hat{\omega} \ll N$ (f is the
 260 Coriolis parameter; $\hat{\omega}$ is the intrinsic frequency; and N is the buoyancy frequency), the zonal and
 261 meridional components of vertical GW momentum flux (MF_x, MF_y) can be derived as

$$(MF_x, MF_y) = -\frac{\rho}{2} \left(\frac{g}{N}\right)^2 \left(\frac{|T'|}{\bar{T}}\right)^2 \left(\frac{k}{m}, \frac{l}{m}\right) \quad (1)$$

262 where ρ is atmospheric density, and g is the acceleration due to gravity (Ern et al., 2004). To
 263 preserve the direction of (MF_x, MF_y) , the three components (k, l, m) of a wave vector are
 264 computed as signed values (Alexander et al., 2018).
 265

266 **3 Results**

267 **3.1 Global Features of GW Amplitudes and Momentum Fluxes**

268 Global distributions of GW amplitudes and momentum fluxes are described in this
 269 section with a comparison between AIRS observations and JAGUAR hindcasts. Prior to that, we
 270 briefly give an overview of the evolution of the zonal wind field during the period of interest. We
 271 do this because the background wind field, which changed drastically due to the SSW, is
 272 expected to be highly correlated with GW characteristics. Figure 1 shows horizontal maps of the
 273 zonal wind at $z = 39$ km during 15–22 December 2018 (Period 1) in Fig. 1a, 23–31 December
 274 2018 (Period 2) in Fig. 1b, and 1–8 January 2019 (Period 3) in Fig. 1c. All the horizontal maps in
 275 this paper are shown for $z = 39$ km, which lies in the center of the usable height range of AIRS
 276 data. The onset of the major warming occurred on 1 January 2019. During Period 1 (Fig. 1a), the
 277 eastward jet in the winter Northern Hemisphere is still strong. The polar vortex has shifted away
 278 from North America towards Europe. It has been shown previously that the Arctic polar vortex is
 279 inclined to be displaced towards the Eurasian Continent especially in recent years (e.g., Zhang et

280 al., 2016), and thus the zonal wind in Period 1 displays a pattern and strength that are similar to
 281 climatological boreal winters. In Period 2 from 23 December to just prior to the SSW onset (Fig.
 282 1b), the polar vortex is located over the North Atlantic. The zonal wind in the Northern
 283 Hemisphere has zonally asymmetric structure with a zonal wavenumber $s=1$. The summer
 284 westward jet at $\sim 25^\circ$ S is stronger than that in Period 1. After the onset of the major warming, or
 285 in Period 3 (Fig. 1c), westward wind has become dominant at high latitudes in the Northern
 286 Hemisphere. The summer jet has been continuously accelerated until this period.

287 Figure 2 displays the horizontal distribution of the amplitudes and momentum fluxes of
 288 stratospheric GWs in Period 1 from AIRS (Figs. 2a, 2c and 2e) and JAGUAR with the AIRS
 289 observational filter applied (Figs. 2b, 2d and 2f). The right-hand panel of each horizontal map
 290 shows the respective zonal-mean values. What stands out in this figure is the good agreement of
 291 the distribution and magnitude of peaks in the amplitudes between JAGUAR and AIRS data.
 292 High GW activities are distributed along the eastward jet in the Northern Hemisphere (Fig. 1a)
 293 and in the low-latitude region of the Southern Hemisphere. There are remarkably large
 294 amplitudes of ~ 3.5 K above the central and eastern Eurasia. This feature is quantitatively
 295 consistent between the model and the observations. Large amplitudes are also observed above
 296 Europe and the highest areas of the Ural mountains in Russia ($\sim 65^\circ$ N, 60° E). The maxima of
 297 these features are 3–3.5 K in the AIRS observation and 2–2.5 K in the JAGUAR data. At low
 298 latitudes ($\sim 20^\circ$ S) in the summer hemisphere, high-amplitude peaks can be seen in the eastern
 299 part of Southern America and near Madagascar Island. There is a background amplitude level of
 300 ~ 1.4 K in AIRS data which is almost uniform everywhere except in the areas of large amplitudes
 301 described above. This level shift is much smaller, specifically ~ 0.5 K, in the JAGUAR data,
 302 which may suggest that the method used of adding noise in the local-area study by Hindley et al
 303 (2019) is not well-suited for this purpose at global scales.

304 As shown in Figs. 2c and 2d, strong westward momentum flux is observed along the
 305 winter jet over the Eurasian Continent. Again, the peaks in this region from JAGUAR data show
 306 good quantitative agreement with the AIRS observations. In the low-latitude region in the
 307 Southern Hemisphere, there is eastward momentum flux both in the AIRS and JAGUAR data.
 308 The magnitude of this eastward momentum flux in eastern South America is slightly smaller in
 309 the JAGUAR data than in the AIRS observations. The zonal-mean MF_x at $\sim 20^\circ$ S is slightly
 310 larger in the results derived from the AIRS observations, with a value of ~ 0.3 mPa in the AIRS
 311 result and ~ 0.2 mPa in the JAGUAR result. The geographical pattern of meridional momentum
 312 flux is also mostly consistent between JAGUAR and AIRS. To the south (north) of the winter jet,
 313 meridional momentum flux is northward (southward) (Figs. 2e and 2f).

314 During 23–31 December 2018 (Period 2), as can be seen in Fig. 3, GW amplitudes and
 315 momentum fluxes in the Northern Hemisphere are much smaller than those during Period 1. On
 316 the other hand, eastward momentum flux at low latitudes in the Southern Hemisphere is slightly
 317 stronger than that in Period 1. These trends are continuously observed in Period 3 as well, as
 318 shown in Fig. 4.
 319

320 3.2 The Observational Filter of AIRS

321 To estimate influence of the AIRS observational filter on the above AIRS results,
 322 comparisons of the amplitudes and momentum fluxes are made here between JAGUAR with and
 323 without the observational filter. Figure 5 displays the amplitudes, vertical wavelenghts λ_z , and

324 momentum flux of stratospheric GWs in Period 1 estimated from the JAGUAR data without the
 325 vertical low-pass filter, which is an analogue of the observational filter of AIRS. Note that the
 326 color scales in Figs. 5a, 5c and 5d are different from those in panels (a, b), (c, d) and (e, f) in Figs.
 327 2–4, respectively. GW amplitudes (Fig. 5a) in the raw model are approximately twice as large as
 328 those with the observational filter applied (Fig. 2b). The same relation applies to the GW
 329 momentum flux (Figs. 5c and 2d; 5d and 2f). The relative variations in the horizontal distribution
 330 of GW amplitudes and momentum flux without the observational filter are similar to those from
 331 AIRS and JAGUAR with the observational filter. Interestingly, however, amplitudes and
 332 momentum fluxes in eastern Eurasia are larger in the results from JAGUAR without the
 333 observational filter. In addition, relatively large amplitudes and poleward momentum fluxes are
 334 observed in the North Atlantic Ocean, which can hardly be seen in the results from AIRS or
 335 JAGUAR with the observational filter.

336 In other words, the most considerable underestimation due to the observational filter is
 337 observed in eastern Eurasia and the North Atlantic Ocean. These areas, denoted by the circles in
 338 Figs. 5a and 5b, correspond to relatively short λ_z (Fig. 5b) along the eastward jet in the Northern
 339 Hemisphere (shown by the dashed curve). Figure 6 shows the polar map of absolute horizontal
 340 wind speed at $z=39$ km ($\sqrt{u^2 + v^2}$, where u and v are zonal and meridional wind) in Period 1.
 341 The areas being discussed here extend from the exit of one of the two jet streaks to the entrance
 342 of the other along the displaced and distorted polar vortex. The background winds in these areas
 343 are weak. Meyer et al. (2018) showed that GW variances observed by AIRS have higher
 344 correlation with background wind speed compared to variances observed by HIRDLS. They
 345 suggested that this is because the Doppler shift increases λ_z of GWs in regions with strong
 346 background winds, making them more easily observed by AIRS, which has lower vertical
 347 resolution. The larger impact of the AIRS observational filter near the exits and entrances of the
 348 jet streaks is consistent with their suggestion.
 349

350 3.3 Case studies

351 To clarify the common features and differences of GWs in the AIRS observation and
 352 JAGUAR data, intercomparisons of T' in three granules are made in this section among AIRS
 353 and JAGUAR with and without the observational filter. Figure 7 displays T' at $z=39$ km
 354 observed nighttime granules over Europe (hereafter Case 1), eastern Eurasia (Case 2), and to the
 355 east of Madagascar (Case 3). In Case 1, the AIRS data and JAGUAR with the observational filter
 356 contains similar wave structures (Figs. 7a and 7b). There are wave-like structure having short
 357 zonal wavelengths to the south of $\sim 48^\circ$ N, and phase fronts laying from south-southwest to
 358 north-northeast to the north of $\sim 51^\circ$ N in both of the data. The amplitudes of these waves are
 359 slightly stronger in the AIRS measurements than in JAGUAR with the observational filter. The
 360 latter wave, which can be seen in the north part of the AIRS granule, is dominant in a larger part
 361 of the result from JAGUAR without the observational filter (Fig. 7c).

362 In Case 2, strong, fine-scale waves whose phase fronts run meridionally are observed to
 363 the south of $\sim 55^\circ$ N both in the AIRS and JAGUAR with the observational filter, as shown in
 364 Figs. 7d and 7e. The overall structure of the temperature perturbations in the filtered JAGUAR
 365 data agrees well with that in the AIRS measurements. In addition to these waves, there are strong
 366 wave fronts bending at a latitude of $\sim 58^\circ$ N in JAGUAR without the observational filter applied

367 (Fig. 7f). The waves composing this V-shaped pattern are not clear in the AIRS measurements or
 368 in JAGUAR with the AIRS observational filter. This difference will be detailed below.

369 The most obvious differences between the AIRS and JAGUAR data are found at low
 370 latitudes in the Southern Hemisphere. The AIRS T' for Case 3 contains a plane wave whose
 371 phase fronts lay from northwest to southeast and a concentric wave whose center is located to the
 372 northwest of the granule (Fig. 7g). However, the plane wave does not have a noticeable
 373 amplitude and only the concentric wave can be seen in the JAGUAR data (Figs. 7h and 7i).

374 To investigate the reason why the V-shaped waves in Case 2 cannot be identified when
 375 the observational filter is applied, we examine the characteristics of the dominant waves in this
 376 V-shaped structure and the background thermodynamical field. Figure 8 provides the results
 377 from the 3-D S-transform of the temperature perturbations in JAGUAR without the observational
 378 filter. Amplitudes are large not only in the south part ($< \sim 55^\circ$ N) but also in the northeast part of
 379 the granule (Fig. 8a). The vertical wavelengths are $\lambda_z = 5\text{--}13$ km in the latter (northeast) region,
 380 which are shorter than the waves in the south region with $\lambda_z \gtrsim 20$ km (Fig. 8b). The distribution
 381 of short λ_z in the full-resolution JAGUAR overlaps the region of small amplitudes in JAGUAR
 382 with the observational filter. This fact is consistent with the low vertical resolution and thus low
 383 sensitivity to waves having short λ_z of AIRS measurements.

384 GW meridional momentum flux to the north (south) of the bending point is southward
 385 (northward), as shown in Fig. 8d. It is noteworthy that eastward (i.e., positive) zonal momentum
 386 flux is observed in the south part of the V-shaped pattern in $z = 32\text{--}41$ km (Figs. 8c and 8g). This
 387 means eastward GWs propagating upward or westward GWs propagating downward are
 388 dominant there.

389 Figure 9 shows the zonal wind and N structure for Case 2. Strong eastward winds are
 390 found at latitudes of $< 58^\circ$ N at $z = \sim 30\text{--}65$ km, while zonal wind is weak on the polar side of 60°
 391 N (Fig. 9a). In the upper stratosphere at $z = 30\text{--}45$ km inside the polar vortex, large N is observed
 392 as shown in Fig. 9b. Considering the dispersion relation for GWs having zonal wave vectors
 393 under the midfrequency assumption, $m^2 \approx N^2 / (c - U)^2$ where c is ground-based phase velocity,
 394 short λ_z in small U and large N are a consistent consequence.
 395

396 4 Discussions

397 Overall, JAGUAR has good skill in reproducing the characteristics of stratospheric GWs
 398 with large amplitudes observed by AIRS. On the other hand, the AIRS GW amplitude has a
 399 background level of 1.2–1.4 K, which is greater than that for the JAGUAR GW amplitude. These
 400 background amplitudes have almost no net contribution to the momentum flux. Hence, it is
 401 inferred that the background level seen in the AIRS amplitude is due to noise. The retrieval noise
 402 we added randomly to the JAGUAR data is not enough to simulate this, likely due to the
 403 uncorrelated nature of the noise source used (see e.g., figure 5.16 of Wright, 2010), and in future
 404 work we will investigate the use of more internally-correlated noise structures.

405 On the polar (equatorial) side of the winter jet, equatorward (poleward) momentum flux
 406 is predominant. This focusing effect of GW rays on the jet can be explained by wave refraction
 407 and advection. When waves propagate westward relative to the background winds, i.e., $\hat{c} =$
 408 $\hat{\omega}/k < 0$ and thus $k < 0$ in the formulation taking $\hat{\omega} > 0$, waves are refracted toward the eastward
 409 jet (e.g., Sato et al., 2009). This is because the time derivative of a meridional wavenumber

410 $d_g l/dt$ as measured by an observer moving with the local group velocity is induced by a
 411 meridional shear of the background zonal wind $\partial U/\partial y$ as:

$$\frac{d_g l}{dt} = -k \frac{\partial U}{\partial y} \quad (2)$$

412 according to ray-tracing theory (Jones, 1969). On the polar side of the eastward jet, negative
 413 $\partial U/\partial y$ decreases l for waves with $k < 0$. As a result, waves propagating upward and westward
 414 relative to U , whose m and k are both negative, tend to have negative MF_y . On the equatorial
 415 side, positive $\partial U/\partial y$ increases l , resulting in $MF_y > 0$. In addition, once the wavevector of a
 416 GW becomes toward the jet axis, the component of the background wind projected in the
 417 direction orthogonal to the wavevector will point to the jet axis. As a result, waves are advected
 418 toward the jet axis (see Fig. 6 of Sato et al., 2012). Since most GW parameterization schemes
 419 ignore lateral propagation of GWs, this focusing of negative MF_x on the jet axis due to refraction
 420 and advection is considered to be one of the causes of the well-known “cold-pole problem”. The
 421 good agreement of the JAGUAR’s GW momentum fluxes along the jet with the AIRS
 422 observations supports the usefulness of this model for studies on this problem.

423 Interestingly, GW amplitudes and momentum fluxes in the low-latitude Southern
 424 Hemisphere increased during SSW development. A possible cause of this is the acceleration of
 425 the westward wind in this region (Fig. 1). The stronger the westward wind is, the larger the
 426 fraction of GWs propagating eastward relative to the background wind can propagate upward.
 427 Several studies have reported that a cooling in the equatorial stratosphere occurs simultaneously
 428 with an SSW (Fritz & Soules, 1970; Julian & Labitzke, 1965). This cooling is induced by strong
 429 planetary wave forcing in the winter stratosphere (e.g., Randel, 1993). This results in
 430 acceleration of the westward wind above and on the polar side of the cooling region due to the
 431 poleward temperature gradient and the thermal wind relationship. Another possible cause is that
 432 more GWs were generated in the tropical troposphere when the SSW occurred. Several studies
 433 found that cooling in the tropical lower stratosphere (e.g., Kodera & Yamada, 2004; Kodera et al.,
 434 2011) and/or upwelling extending in the tropical stratosphere and troposphere itself (Yoshida &
 435 Mizuta, 2021) enhance tropical convection during SSWs. This enhanced convection may have
 436 generated more GWs propagating into the tropical stratosphere. However, we found that there
 437 was no significant long-lasting enhancement in the upwelling at 100 hPa in 5° S–25° S which
 438 persists for as long as the negative MF_x enhancement (not shown). Thus, the acceleration of the
 439 westward jet in the summer stratosphere is a more plausible cause.

440 With regard to GW reproducibility, the comparison with the AIRS observations
 441 demonstrates that the JAGUAR model simulates GW features along the winter jet skillfully.
 442 Relatively speaking, however, larger differences were observed between GWs in the southern
 443 low-latitude region in JAGUAR and those in AIRS. Since the model is a hydrostatic GCM and
 444 cumulus convection is parameterized, GW generation due to convection is not properly
 445 expressed and may be underestimated. The underestimation of convective GWs may be the
 446 reason of the lower GW activity in the summer low-latitude region.

447 Comparing the results from JAGUAR with and without the AIRS observational filter
 448 applied, we showed that the observational filter, or the low vertical resolution of AIRS, reduces
 449 GW amplitudes and momentum fluxes in the model approximately by half. Despite this, the
 450 impact on the relative horizontal distribution of GW characteristics was limited. This finding

451 consistent with that of Meyer et al. (2018) who compared GWs in AIRS measurements with
 452 those in HIRDLS measurements.

453 The most interesting aspect of our results on the impact of the observational filter is that
 454 more GWs were filtered out near the exits and entrances of the two jet streaks. The exit of a jet
 455 streak is the place where spontaneous-adjustment emission of GWs occurs (e.g., Dörnbrack et al.,
 456 2018; Plougonven and Zhang, 2014; Yasuda et al., 2015). In Case 2 in Section 3.3, the eastward
 457 MF_x observed near the jet (Figs. 8c and 8g) suggests downward propagation of westward GWs,
 458 considering the background wind is eastward. This fact indicates that these waves originate from
 459 the jet. The V-shaped phase fronts of these waves shown in Fig. 7f are similar to theoretically-
 460 derived phase structure of GWs emitted from spontaneous adjustment. Then, why did these
 461 waves have short λ_z , which are filtered out by the observational filter? In general, around the exit
 462 or entrance of a jet streak, horizontal wind is not as strong as in the jet core. The static stability
 463 N^2 is high in the middle and upper stratosphere inside the polar vortex due to the GW-driven
 464 winter polar stratopause. In addition, a Q-vector convergence exists on the polar side of the jet
 465 exit region, which induces upwelling. This upwelling may contribute to the formation of high N^2
 466 above. These weak horizontal winds and high N^2 make λ_z of GWs shorter, making it difficult to
 467 resolve them with AIRS. Regarding the background winds and N^2 , conditions in both the exit
 468 and entrance regions of jet streaks are almost the same. In the exit regions of jet streaks, the wave
 469 capture mechanism may also contribute to the small λ_z (Bühler & McIntyre, 2005). According to
 470 this mechanism, GWs heading for the jet exit come to have large negative (positive) vertical
 471 wavenumbers on the top (bottom) edge of the exit of a jet streak, regardless of their source
 472 structure.
 473

474 **5 Summary and Concluding Remarks**

475 A comparison of stratospheric GWs in the GW-permitting GCM, JAGUAR with 3-D
 476 temperature measurements by AIRS has been made for the period of 15 December 2018–8
 477 January 2019. The two datasets show surprisingly good quantitative agreement in:

- 478 1. The peaks in the amplitudes and zonal and meridional momentum fluxes of GWs
- 479 2. The distribution of GW characteristics: high GW activity in Europe, over the Ural
 480 Mountains, in eastern Eurasia, and in the low-latitude region in the summer hemisphere
- 481 3. The attenuation and reinforcement of GWs along the winter eastward jet and summer
 482 westward jet during the SSW occurrence, respectively

483 At the same time, some differences have also been observed:

- 484 4. The results indicate that GWs at low latitudes are underestimated by JAGUAR. A
 485 possible reason for this is that the model cannot sufficiently reproduce convective GWs.
- 486 5. The background level in the AIRS GW amplitudes cannot be fully explained by the
 487 retrieval noise added to JAGUAR GWs. There is almost no net momentum flux
 488 associated with the background amplitudes. We hypothesize that this is due to the
 489 internally-uncorrelated nature of the noise added.

490 Regarding (4), this may be due to low reproducibility of convection in the model. JAGUAR is a
 491 hydrostatic model, and a cumulus parameterization scheme is adopted in it. In general,
 492 cumulus parameterizations are not designed to reproduce GW generation associated with

493 convection, which can be a reason for the low GW activity at low latitudes in the model. Further
494 research using a non-hydrostatic and cloud-resolving model would be interesting to assess the
495 impact of the model configuration of JAGUAR on the GW reproducibility.

496 The influence of the AIRS observational filter has been also estimated by comparing the
497 model results with and without the filter applied. Approximately half of the GW amplitude in the
498 full-resolution JAGUAR was filtered out by the observational filter. At large scales, the relative
499 horizontal distribution was not dramatically changed. However, the regions of large GW
500 amplitude near the entrances or exits of the eastward jet streaks are affected strongly by the
501 observational filter. It has been reported that GWs are generated by spontaneous adjustment near
502 the exit of a jet streak (e.g., Dörnbrack et al., 2018). Conducting a case study, we found that the
503 distribution of V-shaped GWs near the jet exit, which were filtered out due to short λ_z , matched
504 with the regions of weak zonal wind and high N^2 . These two conditions, weak winds and high
505 N^2 , are likely to be met on the polar side of the polar vortex in the middle and upper stratosphere.
506 These results suggest that studies on spontaneous-adjustment emission of GWs using AIRS
507 observations need to pay attention to this aspect.

508 Notwithstanding the limitation that the results have been described only for one boreal
509 winter, the validation of the JAGUAR model we made here supports the effectiveness of this
510 model for various studies on GWs in the middle atmosphere. Performing multi-year hindcast
511 simulations with the model could produce the climatological dataset of the GW momentum flux
512 in the whole middle atmosphere. Such a dataset, validated by comparison with long-term
513 observations, would be a useful guideline for the source parameters in non-orographic GW
514 parameterizations.

515

516 Acknowledgments

517 This work was supported by JSPS KAKENHI Grant Numbers JP21J20798 supporting H. Okui
518 and JP22H00169 supporting H. Okui and K. Sato, by Royal Society University Research
519 Fellowship URF\R\221023 and Research Grant RGF\R1\180010 supporting C. J. Wright, and by
520 NERC grants NE/S00985X/1 and NE/W003201/1 supporting C. J. Wright and N. Hindley.

521

522 Open Research

523 The AIRS temperature data set is derived using AIRS radiances, which are freely available from
524 NASA's GES DISC at <https://disc.gsfc.nasa.gov/> website, by the retrieval method described in
525 Hoffmann and Alexander (2009). The processed AIRS data and JAGUAR hindcast outputs are
526 available from https://pansy.eps.s.u-tokyo.ac.jp/archive_data/Okui_etal_AIRS_2023/. R2022b
527 version of the MATLAB used for spectral analysis of gravity waves and producing figures is
528 presented at <https://jp.mathworks.com/products/matlab.html>. Figures 1 and 6 were produced
529 using the GFD DENNOU Library (<https://www.gfd-dennou.org/arch/del/del-7.5.1/>).

530

531 References

- 532 Albers, J. R., & Birner, T. (2014). Vortex Preconditioning due to Planetary and Gravity Waves
533 prior to Sudden Stratospheric Warmings. *Journal of the Atmospheric Sciences*, **71**(11),
534 4028–4054. <https://doi.org/10.1175/JAS-D-14-0026.1>
- 535 Alexander, M. J., & Barnett, C. (2007). Using Satellite Observations to Constrain
536 Parameterizations of Gravity Wave Effects for Global Models, *Journal of the*
537 *Atmospheric Sciences*, **64**(5), 1652–1665. <https://doi.org/10.1175/JAS3897.1>
- 538 Alexander P., Schmidt T., & de la Torre, A. (2018). A method to determine gravity wave net
539 momentum flux, propagation direction, and “real” wavelengths: A GPS radio
540 occultations soundings case study. *Earth and Space Science*, **5**, 222–230.
541 <https://doi.org/10.1002/2017EA000342>
- 542 Alexander, M. J., & Teitelbaum, H. (2011). Three-dimensional properties of Andes mountain
543 waves observed by satellite: A case study. *Journal of Geophysical Research*, **116**,
544 D23110. <https://doi.org/10.1029/2011JD016151>
- 545 Arakawa, A., & Schubert, W. H. (1974). Interaction of a Cumulus Cloud Ensemble with the
546 Large-Scale Environment, Part I. *Journal of Atmospheric Sciences*, **31**(3), 674–701.
547 [https://doi.org/10.1175/1520-0469\(1974\)031%3C0674:IOACCE%3E2.0.CO;2](https://doi.org/10.1175/1520-0469(1974)031%3C0674:IOACCE%3E2.0.CO;2)
- 548 Aumann, H., Chahine, M., Gautier, C., Goldberg, M., Kalnay, E., McMillin, L., et al. (2003).
549 AIRS/AMSU/HSB on the aqua mission: design, science objectives, data products, and
550 processing systems. *IEEE Transactions on Geoscience and Remote Sensing*, **41**, 253–
551 264. <https://doi.org/10.1109/tgrs.2002.808356>
- 552 Baldwin, M., Gray, L., Dunkerton, T., Hamilton, K., Haynes, P., Randel, W., et al. (2001). The
553 quasi-biennial oscillation. *Reviews of Geophysics*, **39**(2), 179–229.
554 <https://doi.org/10.1029/1999RG000073>
- 555 Barnett, J. J., Hepplewhite, C. L., Osprey, S., Gille, J. C., & Khosravi, R. (2008). Cross-
556 validation of HIRDLS and COSMIC radio occultation retrievals, particularly in relation
557 to fine vertical structure. *Proceedings of SPIE*, **7082**, 708216.
558 <https://doi.org/10.1117/12.800702>
- 559 Becker, E. (2009). Sensitivity of the Upper Mesosphere to the Lorenz Energy Cycle of the
560 Troposphere. *Journal of the Atmospheric Sciences*, **66**(3), 647–666.
561 <https://doi.org/10.1175/2008JAS2735.1>
- 562 Becker, E., & Vadas, S. L. (2018). Secondary gravity waves in the winter mesosphere: Results
563 from a high-resolution global circulation model. *Journal of Geophysical Research:*
564 *Atmospheres*, **123**, 2605–2627. <https://doi.org/10.1002/2017JD027460>
- 565 Becker, E., & Vadas, S. L. (2020). Explicit global simulation of gravity waves in the
566 thermosphere. *Journal of Geophysical Research: Space Physics*, **125**, e2020JA028034.
567 <https://doi.org/10.1029/2020JA028034>
- 568 Becker, E., Vadas, S. L., Bossert, K., Harvey, V. L., Zülicke, C., & Hoffmann, L. (2022). A
569 high-resolution whole-atmosphere model with resolved gravity waves and specified
570 large-scale dynamics in the troposphere and lower stratosphere. *Journal of Geophysical*
571 *Research: Atmospheres*, **127**, e2021JD035018. <https://doi.org/10.1029/2021JD035018>
- 572 Bühler, O., & McIntyre, M. E. (2005). Wave capture and wave–vortex duality. *Journal of Fluid*
573 *Mechanics*, **534**, 67–95. <https://doi.org/10.1017/s0022112005004374>
- 574 Chahine, M. T., Pagano, T. S., Aumann, H. H., Atlas, R., Barnett, C., Blaisdell, J., et al. (2006).
575 AIRS, *Bulletin of the American Meteorological Society*, **87**, 911–926.
576 <https://doi.org/10.1175/bams-87-7-911>

- 577 Chandran, A., Collins, R.L., Garcia, R.R., & Marsh, D. R. (2011). A case study of a
578 spontaneously generated elevated stratopause generated in the Whole Atmosphere
579 Community Climate Model. *Geophysical Research Letters*, **38**, L08804.
580 <https://doi.org/10.1029/2010GL046566>
- 581 Chandran, A., Collins, R. L., Garcia, R. R., Marsh, D. R., Harvey, V. L., Yue, J., and de la Torre,
582 L. (2013). A climatology of elevated stratopause events in the whole atmosphere
583 community climate model. *Journal of Geophysical Research: Atmospheres*, **118**, 1234–
584 1246. <https://doi.org/10.1002/jgrd.50123>
- 585 Dunkerton, T. J. (1997). The role of gravity waves in the quasi-biennial oscillation. *Journal of*
586 *Geophysical Research*, **102**(D22), 26053–26076. <https://doi.org/10.1029/96JD02999>
- 587 Dörnbrack, A., Gisinger, S., Kaifler, N., Portele, T. C., Bramberger, M., Rapp, M., et al. (2018).
588 Gravity waves excited during a minor sudden stratospheric warming, *Atmospheric*
589 *Chemistry and Physics*, **18**, 12915–12931, <https://doi.org/10.5194/acp-18-12915-2018>
- 590 Fritz, S., & Soules, S. D. (1970). Large-scale temperature changes in the stratosphere observed
591 from Nimbus III. *Journal of the Atmospheric Sciences*, **27**, 1091–1097.
592 [https://doi.org/10.1175/1520-0469\(1970\)027%3C1091:LSTCIT%3E2.0.CO;2](https://doi.org/10.1175/1520-0469(1970)027%3C1091:LSTCIT%3E2.0.CO;2)
- 593 Ern, M., Hoffmann, L., & Preusse, P. (2017). Directional gravity wave momentum fluxes in the
594 stratosphere derived from high-resolution AIRS temperature data. *Geophysical*
595 *Research Letters*, **44**, 475–485. <https://doi.org/10.1002/2016GL072007>
- 596 Ern, M., Trinh, Q. T., Preusse, P., Gille, J. C., Mlynczak, M. G., Russell Iii, J. M., & Riese, M.
597 (2018). GRACILE: a comprehensive climatology of atmospheric gravity wave
598 parameters based on satellite limb soundings. *Earth System Science Data*, **10**, 857–892.
599 <https://doi.org/10.5194/essd-10-857-2018>
- 600 Ern, M., Preusse, P., Alexander, M. J., & Warner, C. D. (2004). Absolute values of gravity wave
601 momentum flux derived from satellite data. *Journal Geophysical Research*, **109**,
602 D20103. <https://doi.org/10.1029/2004JD004752>
- 603 Geller, M. A., Alexander, M. J., Love, P. T., Bacmeister, J., Ern, M., Hertzog, A., et al. (2013).
604 A Comparison between Gravity Wave Momentum Fluxes in Observations and Climate
605 Models. *Journal of Climate*, **26**(17), 6383–6405. [https://doi.org/10.1175/jcli-d-12-](https://doi.org/10.1175/jcli-d-12-00545.1)
606 [00545.1](https://doi.org/10.1175/jcli-d-12-00545.1)
- 607 GFD Dennou Club. (2018). Dennou Club Library (version 7.3.4) [Software]. Retrieved from
608 <https://www.gfd-dennou.org/library/dcl/>
- 609 Gille, J., Barnett, J., Whitney, J., Dials, M., Woodard, D., Rudolf, W., Lambert, A., & Mankin,
610 W. (2003). The High Resolution Dynamics Limb Sounder (HIRDLS) Experiment on
611 Aura. *Proceedings of SPIE*, **5152**, 162–171.
- 612 Gille, J. C., Barnett, J., Arter, P., Barker, M., Bernath, P., Boone, C., et al. (2008). High
613 Resolution Dynamics Limb Sounder: Experiment overview, recovery, and validation of
614 initial temperature data. *Journal of Geophysical Research*, **113**, D16S43.
615 <https://doi.org/10.1029/2007JD008824>
- 616 Hersbach, H., Bell, B., Berrisford, P., Hirahara, S., Horányi, A., Muñoz-Sabater, J., et al.
617 (2020). The ERA5 global reanalysis. *Quarterly Journal of the Royal Meteorological*
618 *Society*. **146**, 1999–2049. <https://doi.org/10.1002/qj.3803>
- 619 Hindley, N. P., Wright, C. J., Gadian, A. M., Hoffmann, L., Hughes, J. K., Jackson, D. R., et al.
620 (2021). Stratospheric gravity waves over the mountainous island of South Georgia:
621 testing a high-resolution dynamical model with 3-D satellite observations and

- 622 radiosondes. *Atmospheric Chemistry and Physics*, **21**, 7695–7722.
623 <https://doi.org/10.5194/acp-21-7695-2021>
- 624 Hindley, N. P., Wright, C. J., Hoffmann, L., Moffat-Griffin, T., & Mitchell, N. J. (2020). An 18-
625 year climatology of directional stratospheric gravity wave momentum flux from 3-D
626 satellite observations. *Geophysical Research Letters*, **47**, e2020GL089557.
627 <https://doi.org/10.1029/2020GL089557>
- 628 Hindley, N. P., Wright, C. J., Smith, N. D., Hoffmann, L., Holt, L. A., Alexander, M. J., Moffat-
629 Griffin, T., & Mitchell, N. J. (2019). Gravity waves in the winter stratosphere over the
630 Southern Ocean: high-resolution satellite observations and 3-D spectral analysis.
631 *Atmospheric Chemistry and Physics*, **19**, 15377–15414. [https://doi.org/10.5194/acp-19-](https://doi.org/10.5194/acp-19-15377-2019)
632 [15377-2019](https://doi.org/10.5194/acp-19-15377-2019)
- 633 Hoffmann, L., & Alexander, M. J. (2009). Retrieval of stratospheric temperatures from
634 Atmospheric Infrared Sounder radiance measurements for gravity wave studies. *Journal*
635 *of Geophysical Research*, **114**, D07105. <https://doi.org/10.1029/2008JD011241>
- 636 Hoffmann, L., Alexander, M. J., Clerbaux, C., Grimsdell, A. W., Meyer, C. I., Rößler, T., &
637 Tournier, B. (2014). Intercomparison of stratospheric gravity wave observations with
638 AIRS and IASI. *Atmospheric Measurement Techniques*, **7**, 4517–4537.
639 <https://doi.org/10.5194/amt-7-4517-2014>
- 640 Jones, W. L. (1969). Ray tracing for internal gravity waves. *Journal of Geophysical Research*,
641 **74**, 2028–2033. <https://doi.org/10.1029/JB074i008p02028>
- 642 Kodera, K., Eguchi, N., Lee, J. N., Kuroda, Y., & Yukimoto, S. (2011). Sudden changes in the
643 tropical stratospheric and tropospheric circulation during January 2009. *Journal of the*
644 *Meteorological Society of Japan*, **89**(3), 283–290. <https://doi.org/10.2151/jmsj.2011-308>
- 645 Kodera, K., Mukougawa, H., & Kuroda, Y. (2011). A General Circulation Model Study of the
646 Impact of a Stratospheric Sudden Warming Event on Tropical Convection. *SOLA*, **7**,
647 197–200. <https://doi.org/10.2151/sola.2011-050>
- 648 Körnich, H., & Becker, E. (2010). A simple model for the interhemispheric coupling of the
649 middle atmosphere circulation. *Advances in Space Research*, **45**(5), 661–668.
- 650 Koshin, D., Sato, K., Kohma, M., & Watanabe, S. (2022). An update on the 4D-LETKF data
651 assimilation system for the whole neutral atmosphere. *Geoscientific Model*
652 *Development*, **15**, 2293–2307. <https://doi.org/10.5194/gmd-15-2293-2022>
- 653 Koshin, D., Sato, K., Miyazaki, K., & Watanabe, S. (2020). An ensemble Kalman filter data
654 assimilation system for the whole neutral atmosphere. *Geoscientific Model*
655 *Development*, **13**, 3145–3177. <https://doi.org/10.5194/gmd-13-3145-2020>
- 656 Kruse, C. G., Alexander, M. J., Hoffmann, L., van Niekerk, A., Polichtchouk, I., Bacmeister, J.
657 T., et al. (2022). Observed and Modeled Mountain Waves from the Surface to the
658 Mesosphere near the Drake Passage. *Journal of the Atmospheric Sciences*, **79**(4), 909–
659 932. <https://doi.org/10.1175/JAS-D-21-0252.1>
- 660 Limpasuvan, V., Y. J. Orsolini, A. Chandran, R. R. Garcia, & A. K. Smith (2016). On the
661 composite response of the MLT to major sudden stratospheric warming events with
662 elevated stratopause. *Journal of Geophysical Research: Atmospheres*, **121**, 4518–4537.
663 <https://doi.org/10.1002/2015JD024401>
- 664 Limpasuvan, V., Richter, J. H., Orsolini, Y. J., Stordal, F., & Kvissel, O.-K. (2012). The roles of
665 planetary and gravity waves during a major stratospheric sudden warming as
666 characterized by WACCM. *Journal of Atmospheric and Solar-Terrestrial Physics*, **78–**
667 **79**, 84–98. <https://doi.org/10.1016/j.jastp.2011.03.004>

- 668 Manney, G. L., Krüger, K., Pawson, S., Minschwaner, K., Schwartz, M. J., Daffer, W. H., et al.
669 (2008). The evolution of the stratopause during the 2006 major warming: Satellite data
670 and assimilated meteorological analyses. *Journal of Geophysical Research*, **113**(D11),
671 D11115. <https://doi.org/10.1029/2007JD009097>
- 672 Manney, G. L., Schwartz, M. J., Krüger, K., Santee, M. L., Pawson, S., Lee, J. N., Daffer, W. H.,
673 Fuller, R. A., & Livesey, N. J. (2009). Aura Microwave Limb Sounder observations of
674 dynamics and transport during the record-breaking 2009 Arctic stratospheric major
675 warming. *Geophysical Research Letters*, **36**, L12815.
676 <https://doi.org/10.1029/2009GL038586>
- 677 MathWorks (2022). MATLAB (Version R2022b). [Software]. Retrieved from
678 <https://jp.mathworks.com/products/matlab.html>
- 679 Meyer, C. I., Ern, M., Hoffmann, L., Trinh, Q. T., & Alexander, M. J. (2018). Intercomparison of
680 AIRS and HIRDLS stratospheric gravity wave observations. *Atmospheric Measurement*
681 *Techniques*, **11**(1), 215–232. <https://doi.org/10.5194/amt-11-215-2018>
- 682 Okui, H., Sato, K., Koshin, D., & Watanabe, S. (2021). Formation of a mesospheric inversion
683 layer and the subsequent elevated stratopause associated with the major stratospheric
684 sudden warming in 2018/19. *Journal of Geophysical Research: Atmospheres*, **126**,
685 e2021JD034681. <https://doi.org/10.1029/2021JD034681>
- 686 Okui, H., Sato, K., & Watanabe, S. (2022). Contribution of gravity waves to universal vertical
687 wavenumber ($\sim m^{-3}$) spectra revealed by a gravity-wave-permitting general circulation
688 model. *Journal of Geophysical Research: Atmospheres*, **127**(10), e2021JD036222.
689 <https://doi.org/10.1029/2021JD036222>
- 690 Plougonven, R., & Zhang, F. (2014). Internal gravity waves from atmospheric jets and fronts.
691 *Reviews of Geophysics*, **52**, 33–76. <https://doi.org/10.1002/2012RG000419>
- 692 Randel, W. J. (1993). Global Variations of Zonal Mean Ozone during Stratospheric Warming
693 Events. *Journal of Atmospheric Sciences*, **50**(19), 3308–3321.
694 [https://doi.org/10.1175/1520-0469\(1993\)050%3C3308:GVOZMO%3E2.0.CO;2](https://doi.org/10.1175/1520-0469(1993)050%3C3308:GVOZMO%3E2.0.CO;2)
- 695 Rao, J., Garfinkel, C. I., Chen, H., & White, I. P. (2019). The 2019 New Year stratospheric
696 sudden warming and its real-time predictions in multiple S2S models. *Journal of*
697 *Geophysical Research: Atmospheres*, **124**, 11155–11174.
698 <https://doi.org/10.1029/2019JD030826>
- 699 Sato, K., & Dunkerton, T. J. (1997). Estimates of momentum flux associated with equatorial
700 Kelvin and gravity waves. *Journal of Geophysical Research*, **102**, 26247–26261.
701 <https://doi.org/10.1029/96JD02514>
- 702 Sato, K., Tateno, S., Watanabe, S., & Kawatani, Y. (2012). Gravity Wave characteristics in the
703 Southern Hemisphere revealed by a high-resolution middle-atmosphere general
704 circulation model. *Journal of the Atmospheric Sciences*, **69**(4), 1378–1396.
705 <https://doi.org/10.1175/jas-d-11-0101.1>
- 706 Sato, K., Watanabe, S., Kawatani, Y., Tomikawa, Y., Miyazaki, K., & Takahashi, M. (2009). On
707 the origins of mesospheric gravity waves. *Geophysical Research Letters*, **36**, L19801.
708 <https://doi.org/10.1029/2009GL039908>
- 709 Siskind, D. E., Eckermann, S. D., McCormack, J. P., Coy, L., Hoppel, K. W., & Baker, N. L.
710 (2010). Case studies of the mesospheric response to recent minor, major, and extended
711 stratospheric warmings. *Journal of Geophysical Research*, **115**, D00N03.
712 <https://doi.org/10.1029/2010JD014114>

- 713 Smith, A. K., Pedatella, N. M., & Mullen, Z. K. (2020). Interhemispheric Coupling Mechanisms
714 in the Middle Atmosphere of WACCM6. *Journal of the Atmospheric Sciences*, **77**(3),
715 1101–1118. <https://doi.org/10.1175/JAS-D-19-0253.1>
- 716 Stockwell, R. G., Mansinha, L., & Lowe, R. P. (1996). Localization of the complex spectrum:
717 The S transform. *IEEE Transactions on Signal Processing*, **44**(4), 998–1001.
718 <https://doi.org/10.1109/78.492555>
- 719 Thurairajah, B., Bailey, S. M., Cullens, C. Y., Hervig, M. E., & Russell, J. M. (2014). Gravity
720 wave activity during recent stratospheric sudden warming events from SOFIE
721 temperature measurements. *Journal of Geophysical Research: Atmospheres*, **119**, 8091–
722 8103, doi:10.1002/2014JD021763.
- 723 Tomikawa, Y., Sato, K., Watanabe, S., Kawatani, Y., Miyazaki, K., & Takahashi, M. (2012).
724 Growth of planetary waves and the formation of an elevated stratopause after a major
725 stratospheric sudden warming in a T213L256 GCM. *Journal of Geophysical Research*,
726 **117**, D16101. <https://doi.org/10.1029/2011JD017243>
- 727 Vadas, S. L., & Becker, E. (2018). Numerical modeling of the excitation, propagation, and
728 dissipation of primary and secondary gravity waves during wintertime at McMurdo
729 Station in the Antarctic. *Journal of Geophysical Research: Atmospheres*, **123**, 9326–
730 9369. <https://doi.org/10.1029/2017JD027974>
- 731 Watanabe, S., Kawatani, Y., Tomikawa, Y., Miyazaki, K., Takahashi, M., & Sato, K. (2008).
732 General aspects of a T213L256 middle atmosphere general circulation model. *Journal*
733 *of Geophysical Research: Atmospheres*, **113**(D12).
734 <https://doi.org/10.1029/2008jd010026>
- 735 Watanabe, S., Koshin, D., Noguchi, S., & Sato, K. (2022). Gravity wave morphology during the
736 2018 sudden stratospheric warming simulated by a whole neutral atmosphere general
737 circulation model. *Journal of Geophysical Research: Atmospheres*, **127**,
738 e2022JD036718. <https://doi.org/10.1029/2022JD036718>
- 739 Watanabe, S., & Miyahara, S. (2009). Quantification of the gravity wave forcing of the migrating
740 diurnal tide in a gravity wave-resolving general circulation model. *Journal of*
741 *Geophysical Research: Atmospheres*, **114**, D07110.
742 <https://doi.org/10.1029/2008JD011218>
- 743 Wright, C. (2010). Detection of stratospheric gravity waves using HIRDLS data [PhD thesis].
744 University of Oxford.
- 745 Wright, C. J., Hindley, N. P., Alexander, M. J., Holt, L. A., & Hoffmann, L. (2021). Using
746 vertical phase differences to better resolve 3D gravity wave structure. *Atmospheric*
747 *Measurement Techniques*, **14**, 5873–5886, <https://doi.org/10.5194/amt-14-5873-2021>
- 748 Wright, C. J., Hindley, N. P., Hoffmann, L., Alexander, M. J., & Mitchell, N. J. (2017).
749 Exploring gravity wave characteristics in 3-D using a novel S-transform technique:
750 AIRS/Aqua measurements over the Southern Andes and Drake Passage. *Atmospheric*
751 *Chemistry and Physics*, **17**, 8553–8575. <https://doi.org/10.5194/acp-17-8553-2017>
- 752 Wright, C. J., Hindley, N. P., & Mitchell, N. J. (2016a). Combining AIRS and MLS observations
753 for three-dimensional gravity wave measurement. *Geophysical Research Letters*, **43**,
754 884–893, <https://doi.org/10.1002/2015GL067233>
- 755 Wright, C. J., Hindley, N. P., Moss, A. C., & Mitchell, N. J. (2016b). Multi-instrument gravity-
756 wave measurements over Tierra del Fuego and the Drake Passage – Part 1: Potential
757 energies and vertical wavelengths from AIRS, COSMIC, HIRDLS, MLS-Aura,

- 758 SAAMER, SABER and radiosondes. *Atmospheric Measurement Techniques*, **9**, 877–
759 908. <https://doi.org/10.5194/amt-9-877-2016>
- 760 Wright, C. J., Osprey, S. M., Barnett, J. J., Gray, L. J., & Gille, J. C. (2010). High Resolution
761 Dynamics Limb Sounder measurements of gravity wave activity in the 2006 Arctic
762 stratosphere. *Journal of Geophysical Research*, **115**, D02105.
763 <https://doi.org/10.1029/2009JD011858>
- 764 Wright, C. J., Rivas, M. B., & Gille, J. C. (2011). Intercomparisons of HIRDLS, COSMIC and
765 SABER for the detection of stratospheric gravity waves. *Atmospheric Measurement
766 Techniques*, **4**, 1581–1591, <https://doi.org/10.5194/amt-4-1581-2011>
- 767 Yasuda, Y., Sato, K., & Sugimoto, N. (2015). A Theoretical Study on the Spontaneous Radiation
768 of Inertia–Gravity Waves Using the Renormalization Group Method. Part I: Derivation
769 of the Renormalization Group Equations. *Journal of the Atmospheric Sciences*, **72**(3),
770 957–983. <https://doi.org/10.1175/JAS-D-13-0370.1>
- 771 Yasui, R., Sato, K., & Miyoshi, Y. (2021). Roles of Rossby Waves, Rossby–Gravity Waves, and
772 Gravity Waves Generated in the Middle Atmosphere for Interhemispheric Coupling.
773 *Journal of the Atmospheric Sciences*, **78**(12), 3867–3888. <https://doi.org/10.1175/JAS-D-21-0045.1>
- 774
- 775 Yoshida, K., & Mizuta, R. (2021). Do sudden stratospheric warmings boost convective activity
776 in the tropics? *Geophysical Research Letters*, **48**, e2021GL093688.
777 <https://doi.org/10.1029/2021GL093688>
- 778 Zhang, J., Tian, W., Chipperfield, M., Xie, F., & Huang, J. (2016). Persistent shift of the Arctic
779 polar vortex towards the Eurasian continent in recent decades. *Nature Climate Change*,
780 **6**, 1094–1099. <https://doi.org/10.1038/nclimate3136>
- 781

782 **Figure 1.** Zonal wind at a geopotential height of $z=39$ km during (a) 15–22 December 2018
 783 (Period 1), (b) 23–31 December 2018 (Period 2), and (c) 1–8 January 2019 (Period 3) obtained
 784 from JAGUAR. An Arctic major SSW occurred on 1 January 2019, the first day of Period 3.
 785

786 **Figure 2.** (a, b) Amplitudes and (c, d) zonal and (e, f) meridional momentum flux of dominant
 787 GWs at $z=39$ km averaged over 15–22 December 2018 (Period 1). Panels (a, c, e) and (b, d, f)
 788 show the results from the AIRS observations and the JAGUAR data, respectively. The right
 789 elongated panels display the zonal mean of the values shown in the respective panels on the left
 790 side.
 791

792 **Figure 3.** As in Fig. 2 but for 23–31 December 2018 (Period 2).
 793

794 **Figure 4.** As in Fig. 2 but for 1–8 January 2019 (Period 3).
 795

796 **Figure 5.** (a) Amplitudes, (b) vertical wavelengths λ_z , and (c) zonal and (d) meridional
 797 momentum flux of dominant GWs at $z=39$ km estimated from the JAGUAR data without the
 798 AIRS observational filter applied. The right elongated panels display the zonal mean of the
 799 values shown in the left respective ones. Note that the color scales for the maps and the
 800 horizontal axes for the curves are different from those in Figs. 2–4. Two circles in panels (a) and
 801 (b) denote the regions where the GW amplitudes are especially large relative to those in the
 802 JAGUAR data with the observational filter (Fig. 2b). A dashed curve in panel (b) represents the
 803 path of the eastward jet, as shown in Fig. 1a.
 804

805 **Figure 6.** North Pole map of the absolute horizontal wind speed averaged over Period 1 obtained
 806 from JAGUAR data. The polar vortex is displaced toward the Eurasian Continent with two jet
 807 streaks from Europe to the Central Asia and from the East Asia to Greenland.
 808

809 **Figure 7.** Temperature perturbations at $z=39$ km in AIRS granules (a–c) in Europe at 1:54 UTC
 810 on 22 December (Case 1), (d–f) in eastern Eurasia at 20:36 UTC on 16 December (Case 2), and
 811 (g–i) to the east of Madagascar at 21:12 UTC on 20 December (Case 3). Panels (a, d, g), (b, e, h),
 812 and (c, f, i) show the results from the AIRS observations, JAGUAR with the observational filter,
 813 and JAGUAR without the observational filter, respectively. Panel (j) provides the location of the
 814 regions shown in panels (a–i) on Fig. 2a.
 815

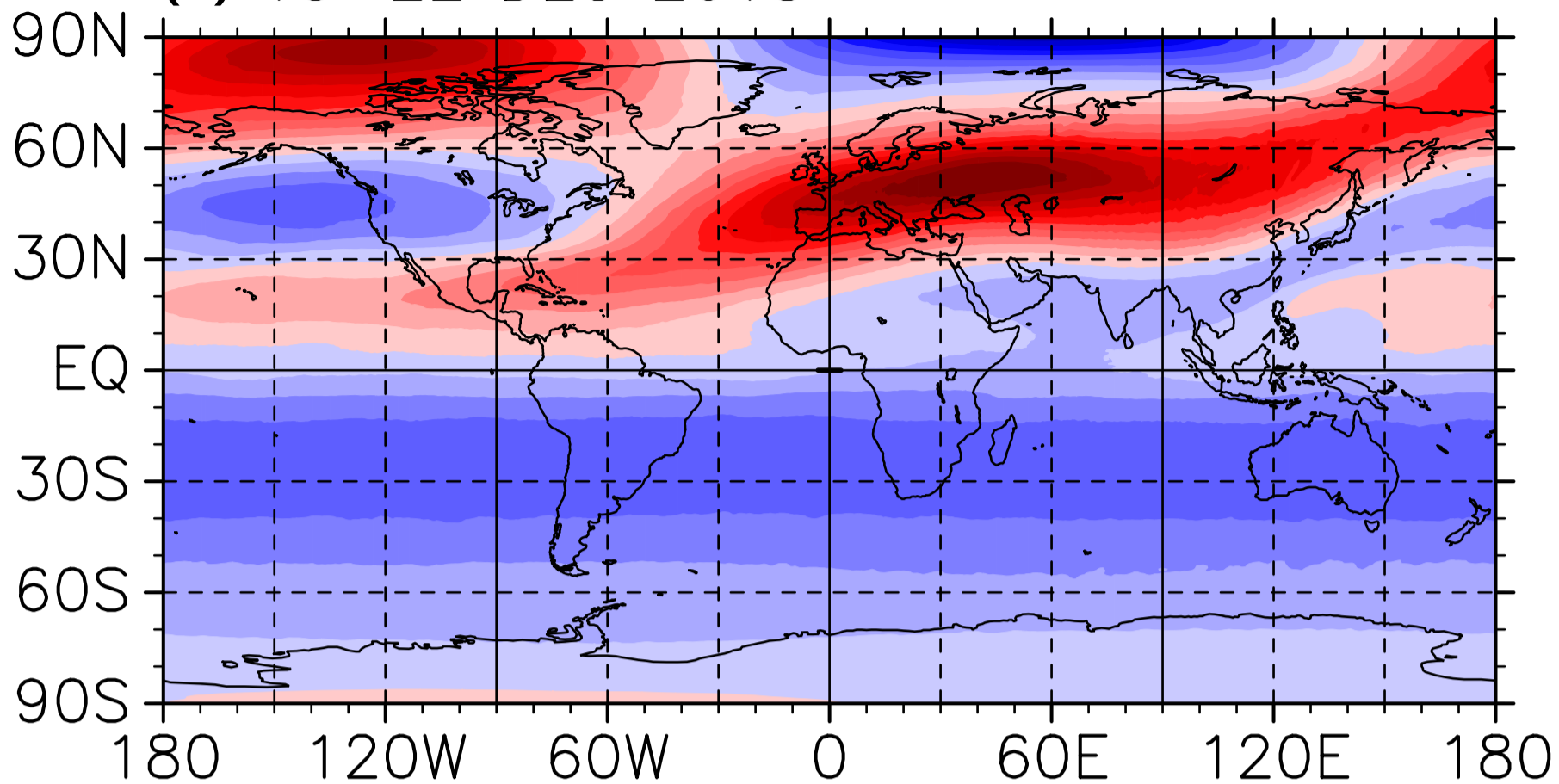
816 **Figure 8.** Results from the 3-D S-transform for Case 2. Panels (a–d) show the horizontal maps at
 817 $z=39$ km and panels (e–h) show the latitude-altitude sections at 105° E of (a, e) amplitudes, (b,
 818 f) λ_z , and (c, g) zonal and (d, h) meridional momentum flux. Vertical (horizontal) lines in the top
 819 (bottom) panels denote the longitude (altitude) of the bottom (top) panels.
 820

821 **Figure 9.** Latitude-altitude section at 105° E of (a) zonal wind and (b) the buoyancy frequency
822 $N = \sqrt{(g/\bar{T})(d\bar{T}/dz)}$ for Case 2 obtained from the JAGUAR data.
823

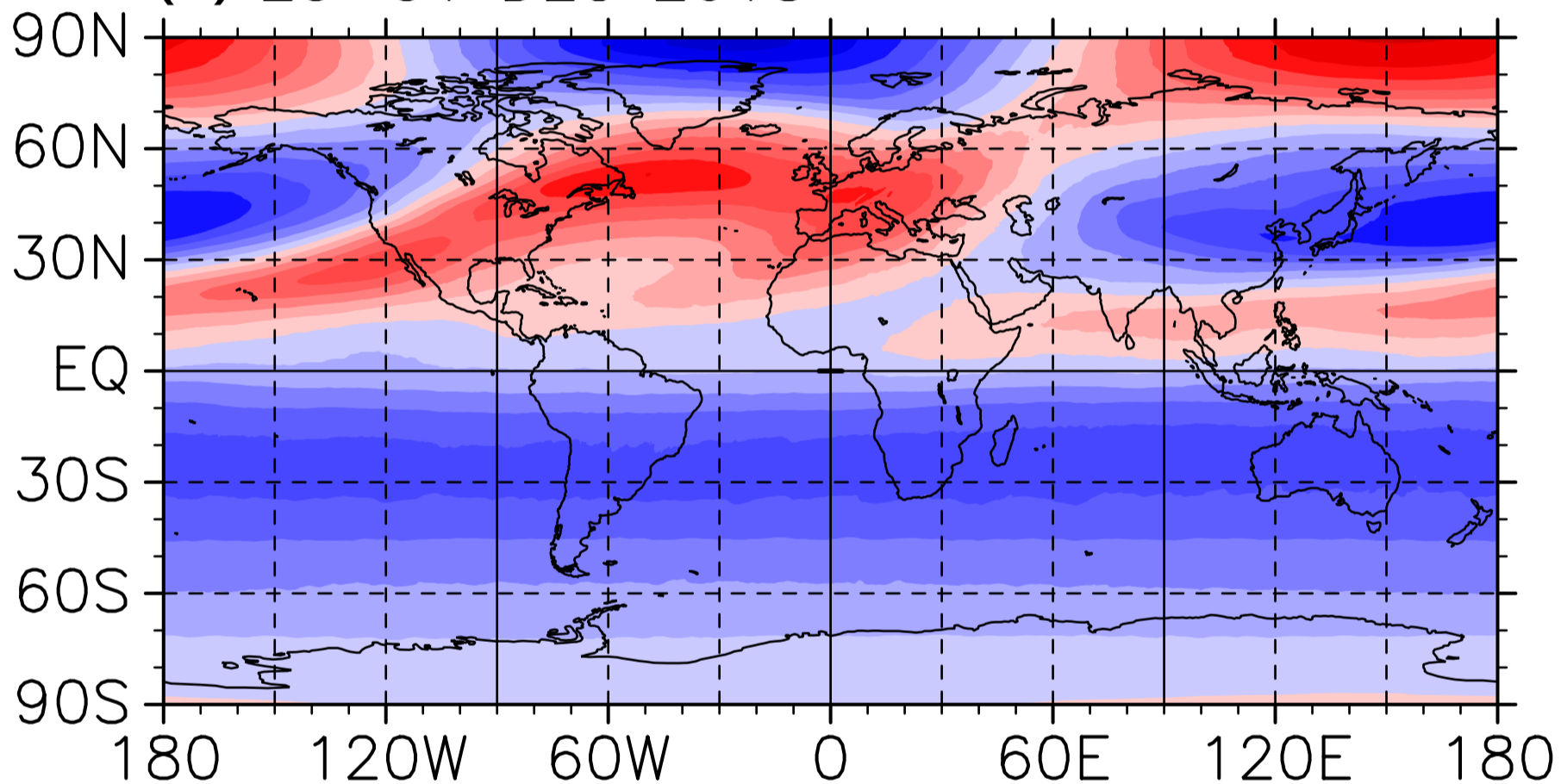
Figure 1.

U at z=39km

(a) 15–22 DEC 2018



(b) 23–31 DEC 2018



(c) 1–8 JAN 2019

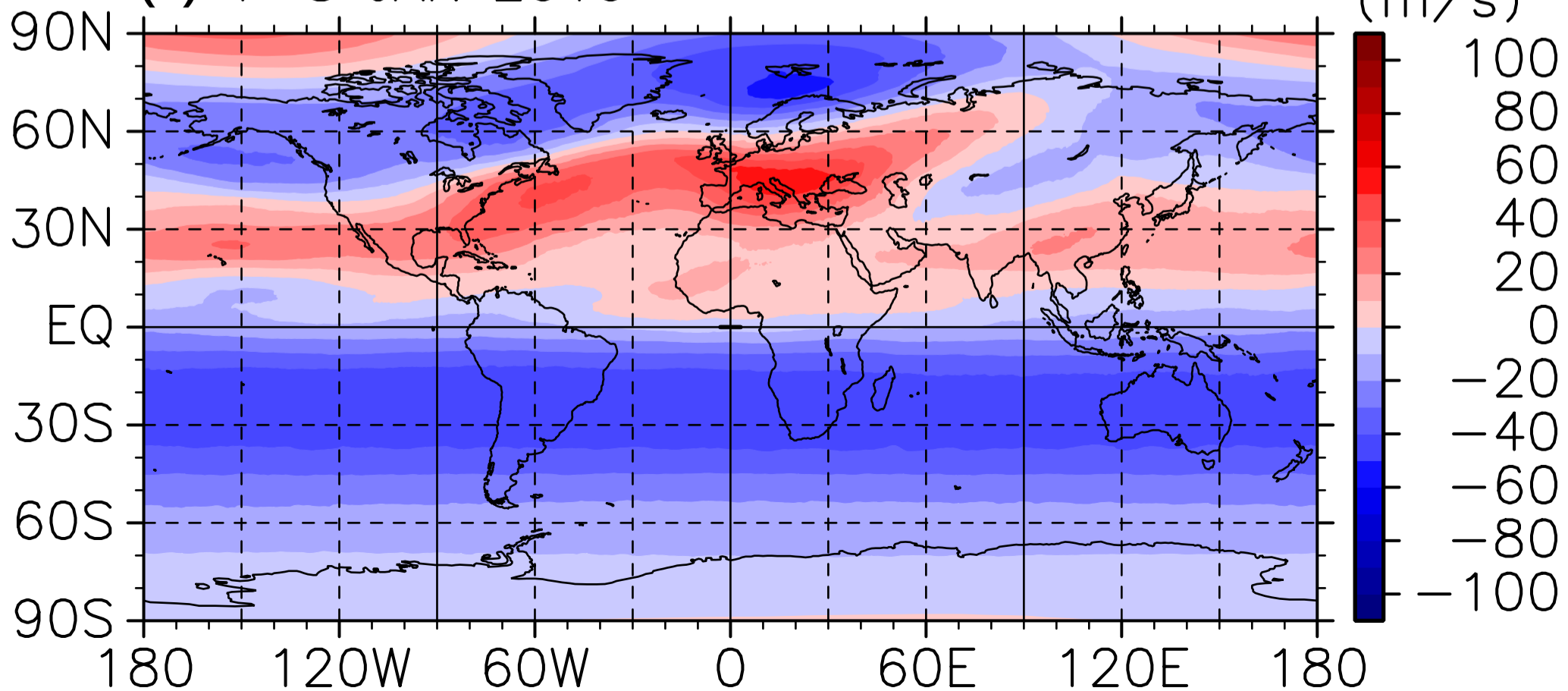
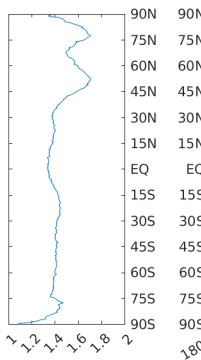
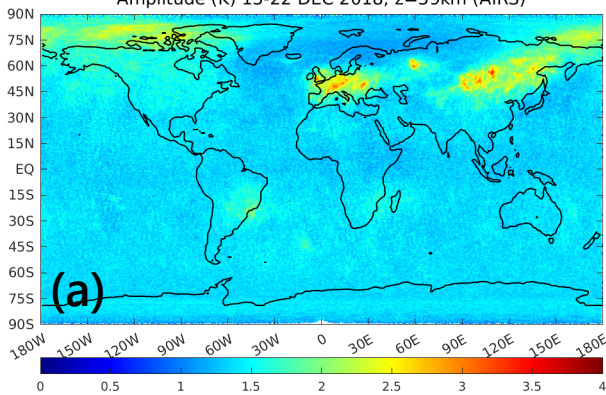
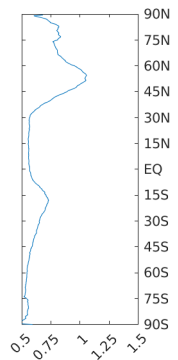
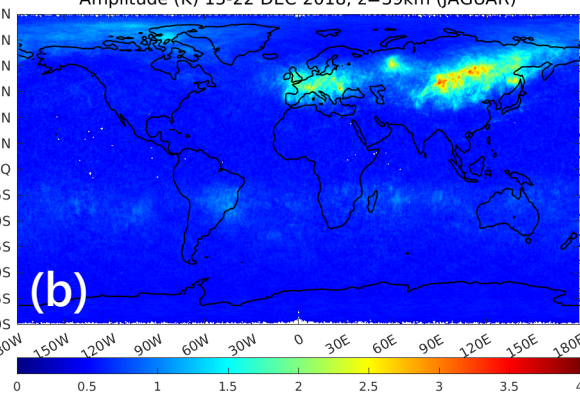


Figure 2.

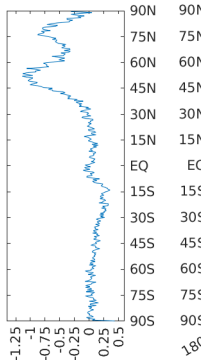
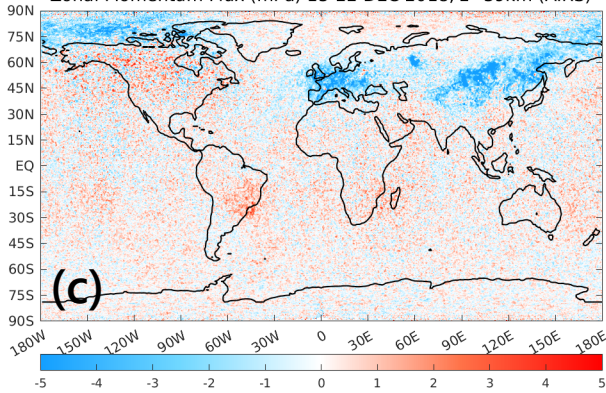
Amplitude (K) 15-22 DEC 2018, z=39km (AIRS)



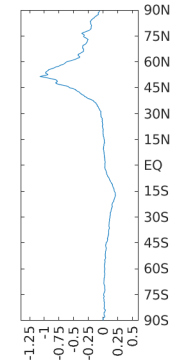
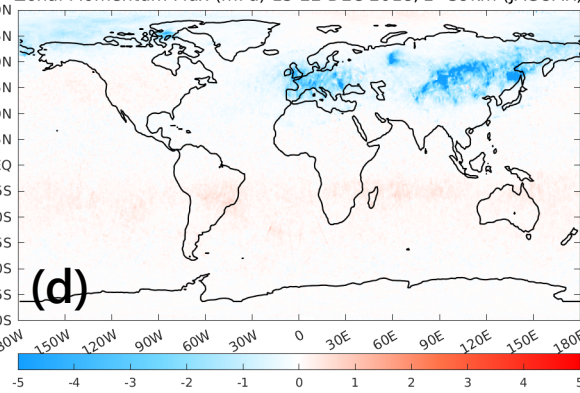
Amplitude (K) 15-22 DEC 2018, z=39km (JAGUAR)



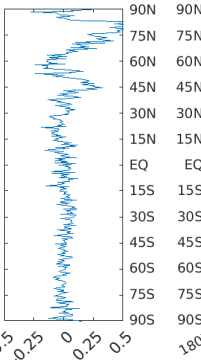
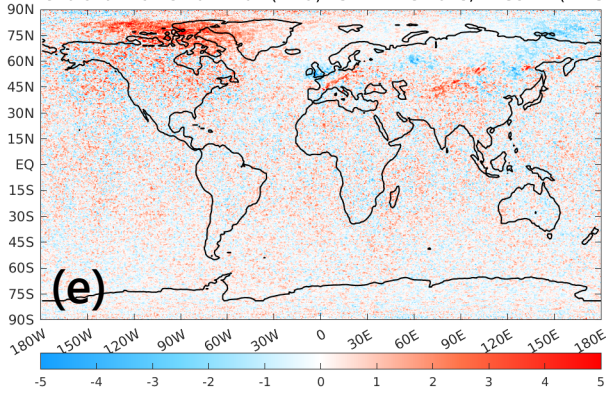
Zonal Momentum Flux (mPa) 15-22 DEC 2018, z=39km (AIRS)



Zonal Momentum Flux (mPa) 15-22 DEC 2018, z=39km (JAGUAR)



Meridional Momentum Flux (mPa) 15-22 DEC 2018, z=39km (AIRS)



Meridional Momentum Flux (mPa) 15-22 DEC 2018, z=39km (JAGUAR)

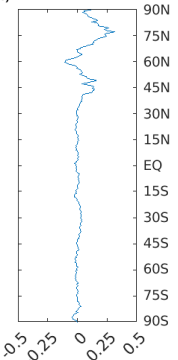
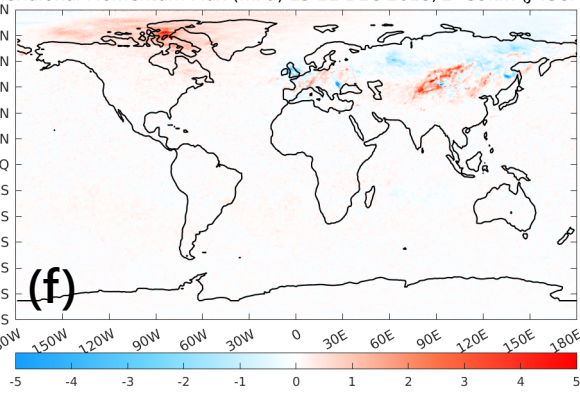
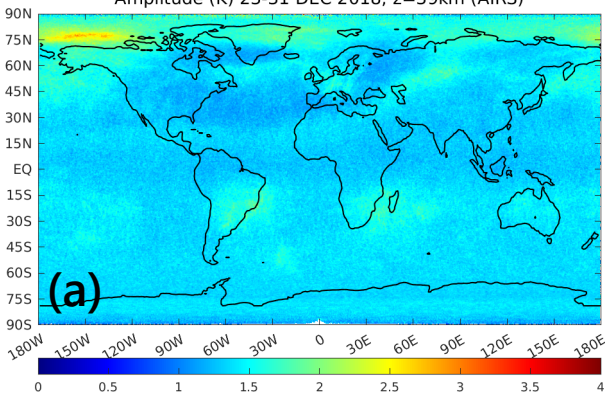


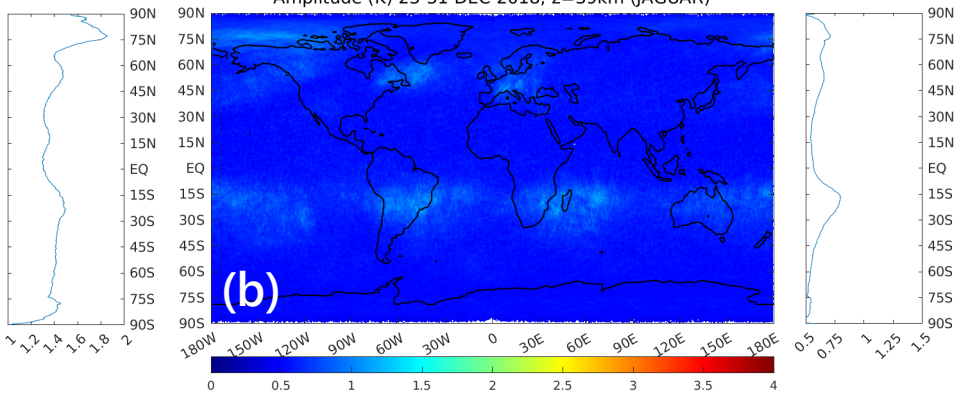
Figure 3.

Amplitude (K) 23-31 DEC 2018, z=39km (AIRS)



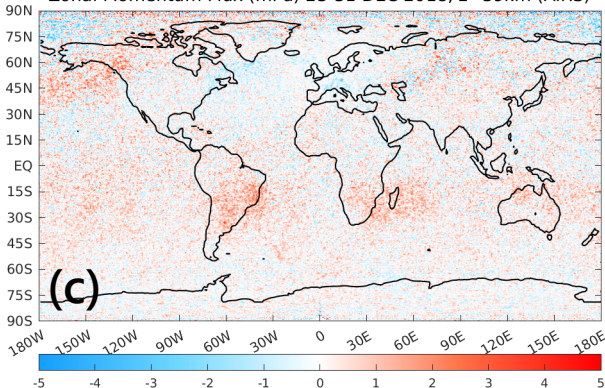
(a)

Amplitude (K) 23-31 DEC 2018, z=39km (JAGUAR)



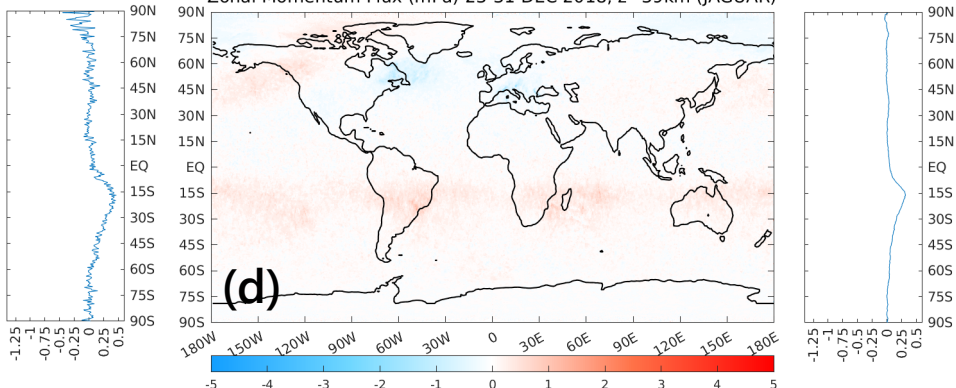
(b)

Zonal Momentum Flux (mPa) 23-31 DEC 2018, z=39km (AIRS)



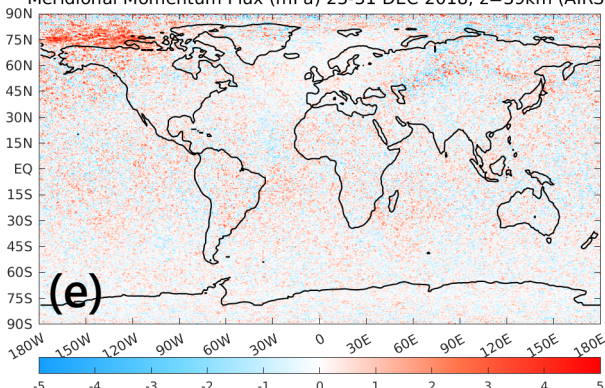
(c)

Zonal Momentum Flux (mPa) 23-31 DEC 2018, z=39km (JAGUAR)



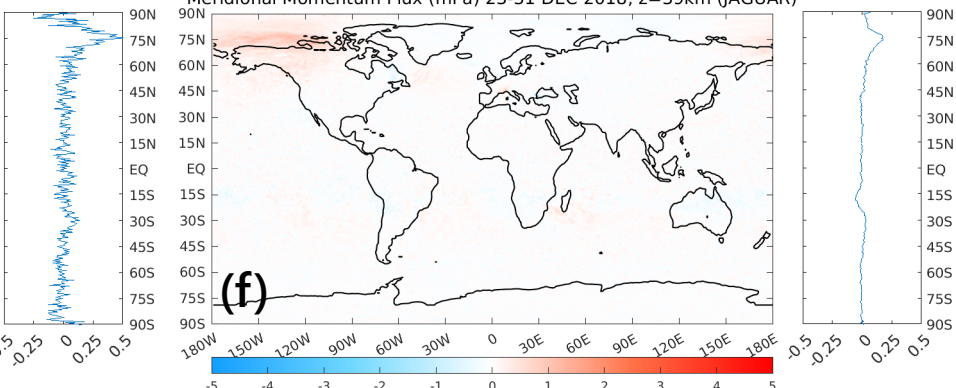
(d)

Meridional Momentum Flux (mPa) 23-31 DEC 2018, z=39km (AIRS)



(e)

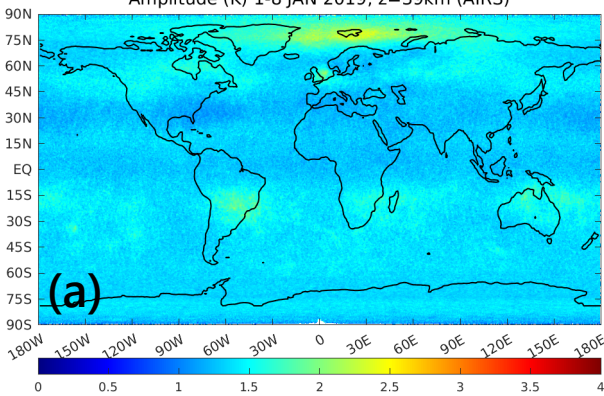
Meridional Momentum Flux (mPa) 23-31 DEC 2018, z=39km (JAGUAR)



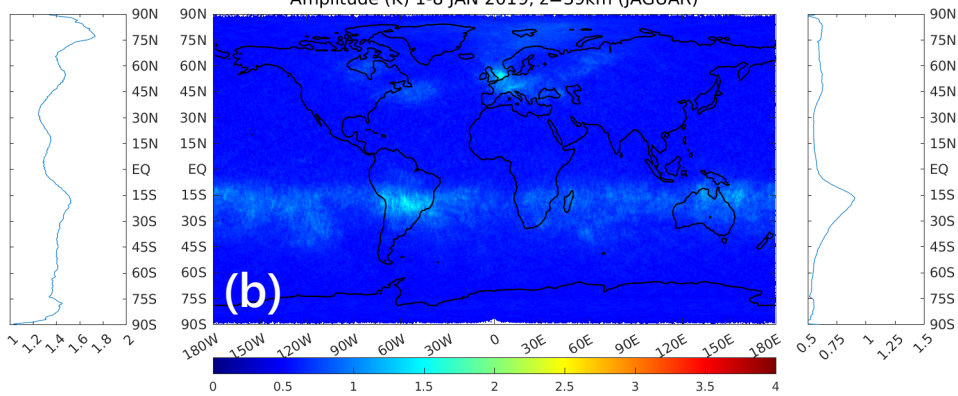
(f)

Figure 4.

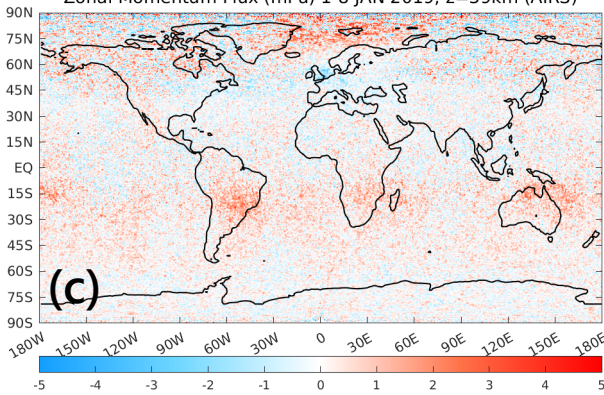
Amplitude (K) 1-8 JAN 2019, z=39km (AIRS)



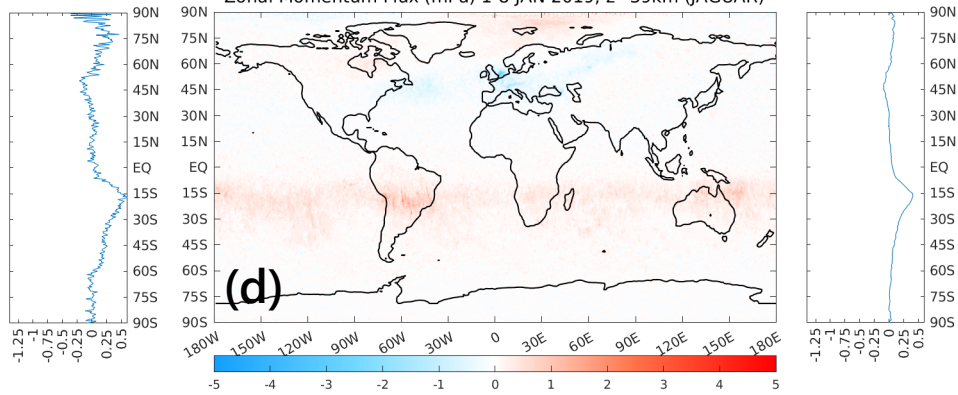
Amplitude (K) 1-8 JAN 2019, z=39km (JAGUAR)



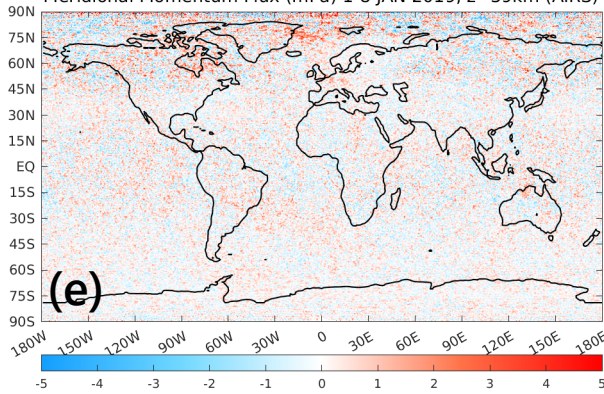
Zonal Momentum Flux (mPa) 1-8 JAN 2019, z=39km (AIRS)



Zonal Momentum Flux (mPa) 1-8 JAN 2019, z=39km (JAGUAR)



Meridional Momentum Flux (mPa) 1-8 JAN 2019, z=39km (AIRS)



Meridional Momentum Flux (mPa) 1-8 JAN 2019, z=39km (JAGUAR)

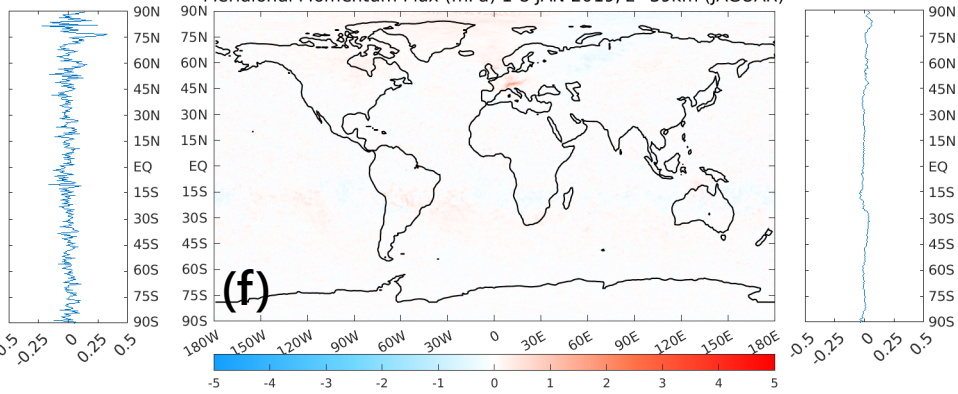
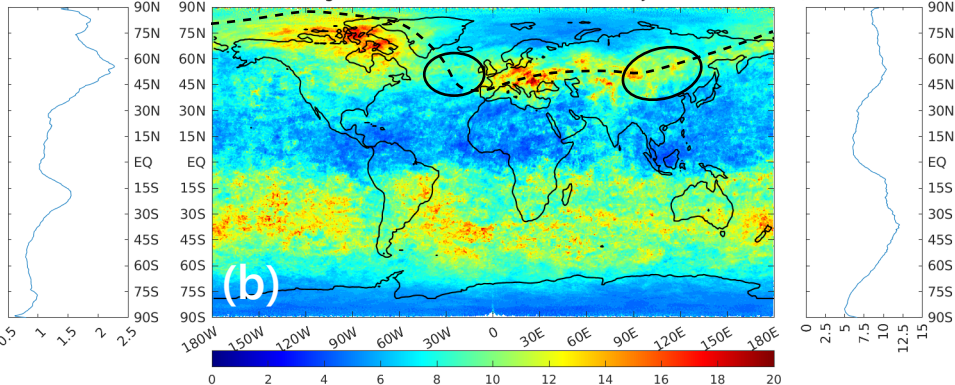
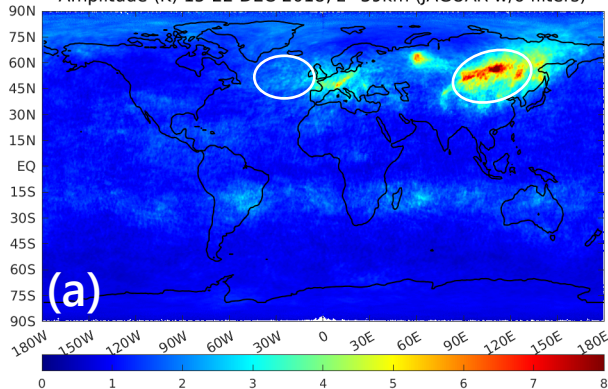
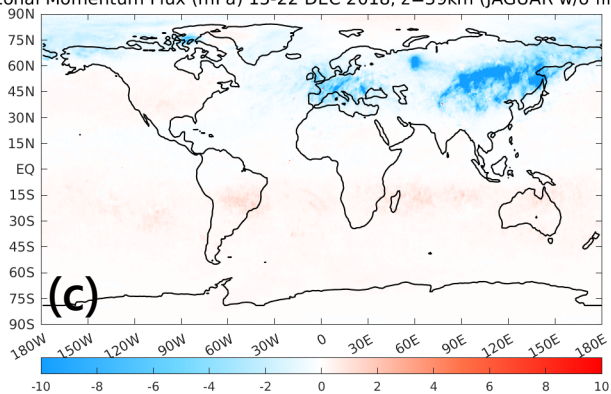


Figure 5.

Amplitude (K) 15-22 DEC 2018, z=39km (JAGUAR w/o filters)



Zonal Momentum Flux (mPa) 15-22 DEC 2018, z=39km (JAGUAR w/o filters)



Meridional Momentum Flux (mPa) 15-22 DEC 2018, z=39km (JAGUAR w/o filters)

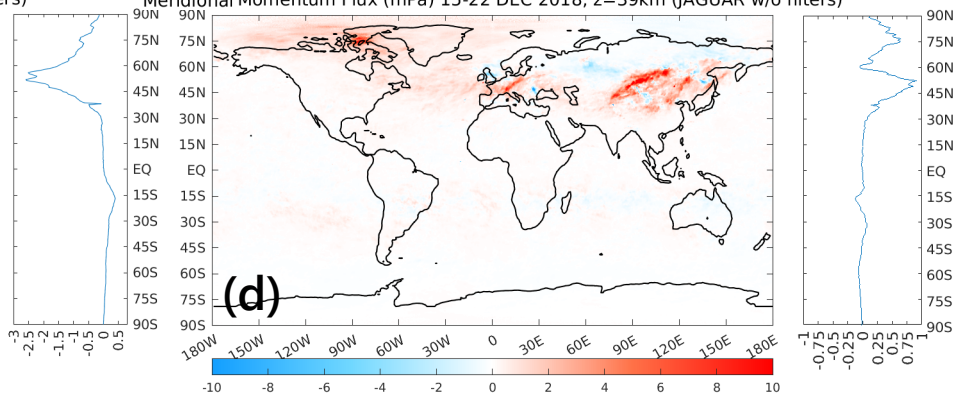


Figure 6.

$|u|$ at $z=39\text{km}$
15–22 DEC 2018

(m/s)

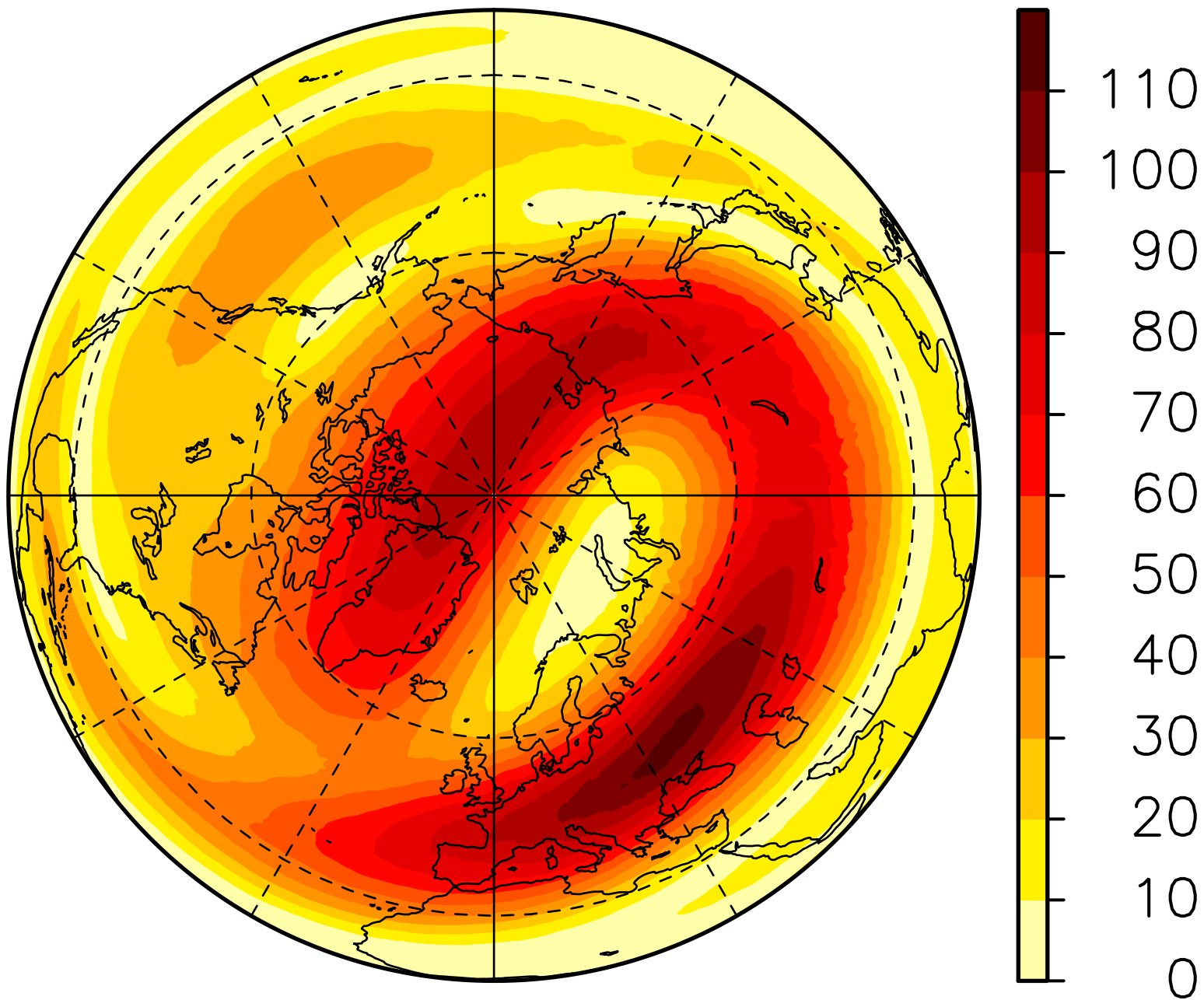
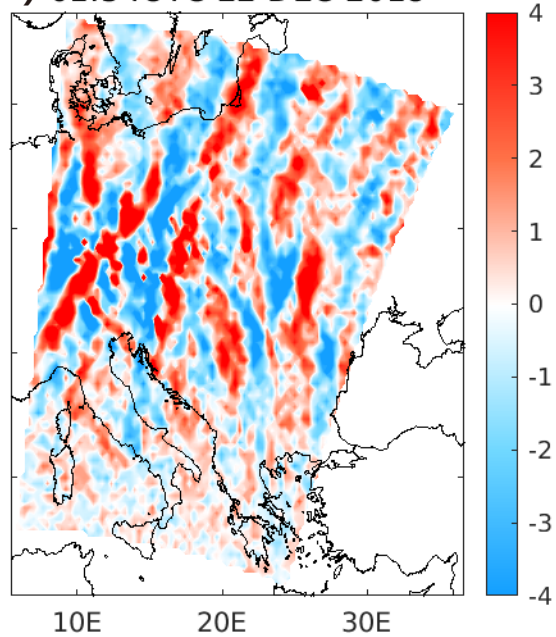
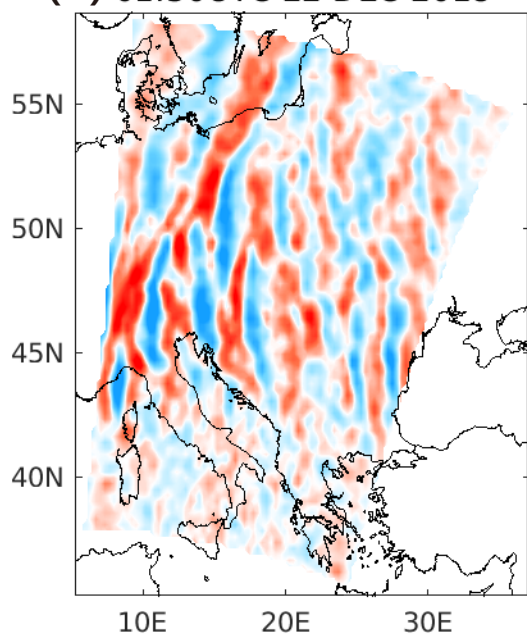


Figure 7.

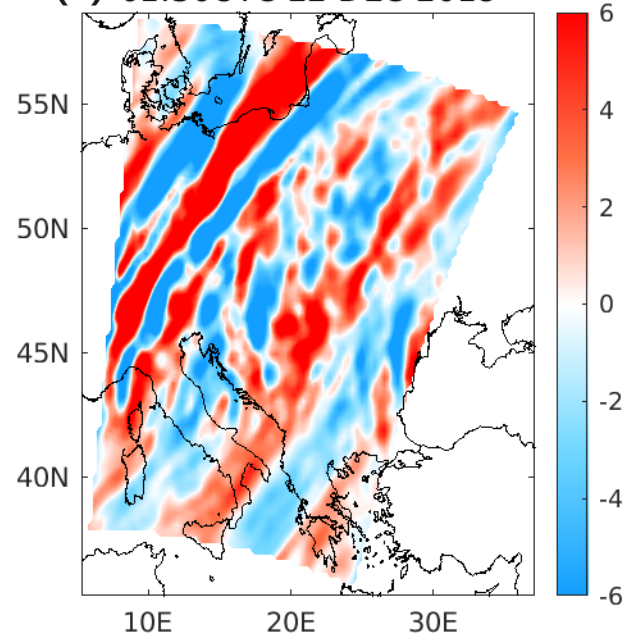
(a) AIRS
01:54UTC 22 DEC 2018



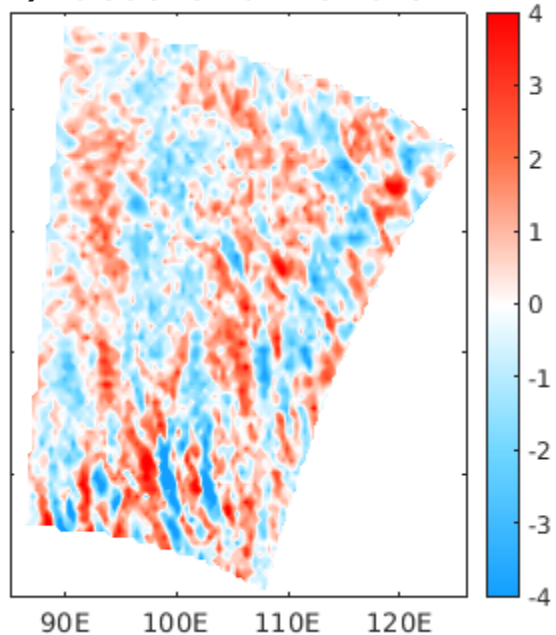
(b) JAGUAR w/ obs. filter
01:30UTC 22 DEC 2018



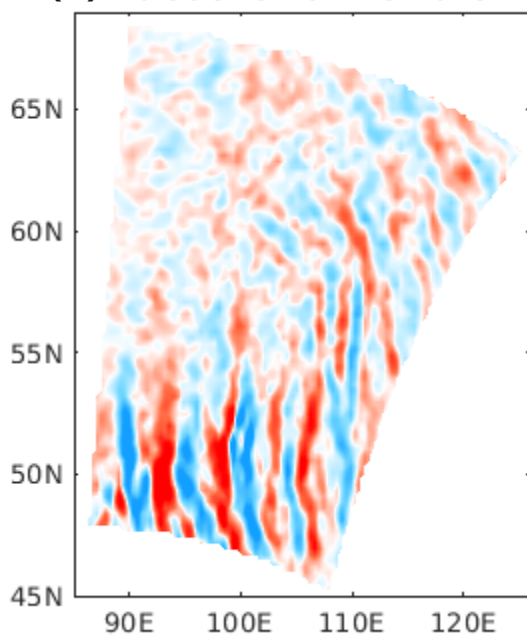
(c) JAGUAR w/o obs. filter
01:30UTC 22 DEC 2018



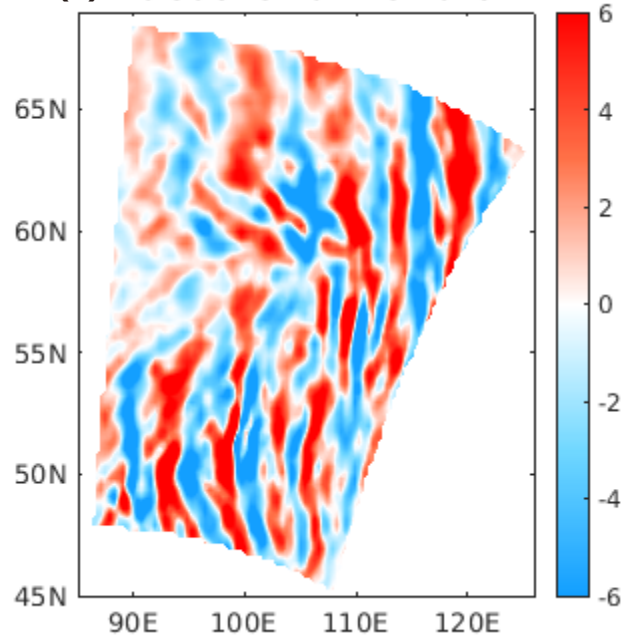
(d) 20:36UTC 16 DEC 2018



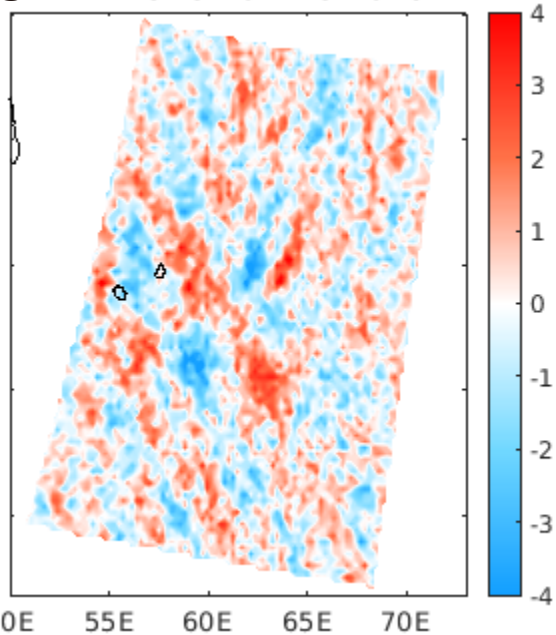
(e) 20:30UTC 16 DEC 2018



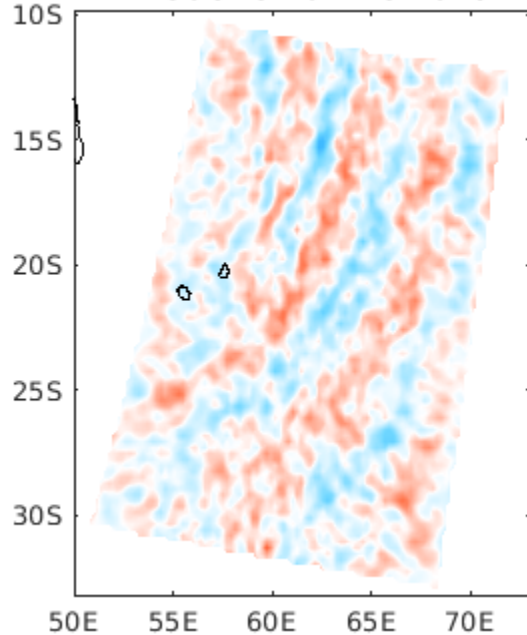
(f) 20:30UTC 16 DEC 2018



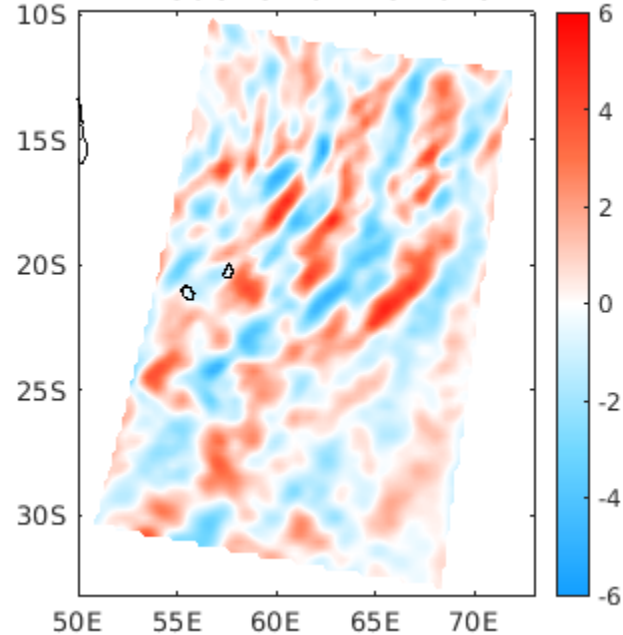
(g) 21:12UTC 20 DEC 2018



(h) 21:30UTC 20 DEC 2018



(i) 21:30UTC 20 DEC 2018



(j) Amplitude (K) 15-22 DEC 2018, z=39km (AIRS)

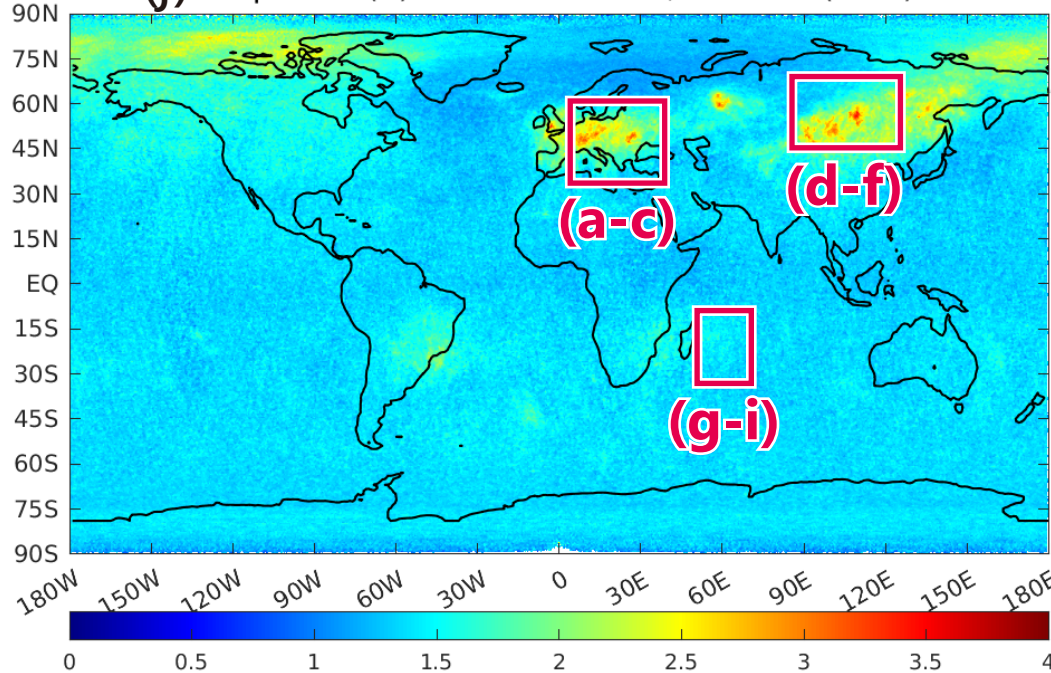


Figure 8.

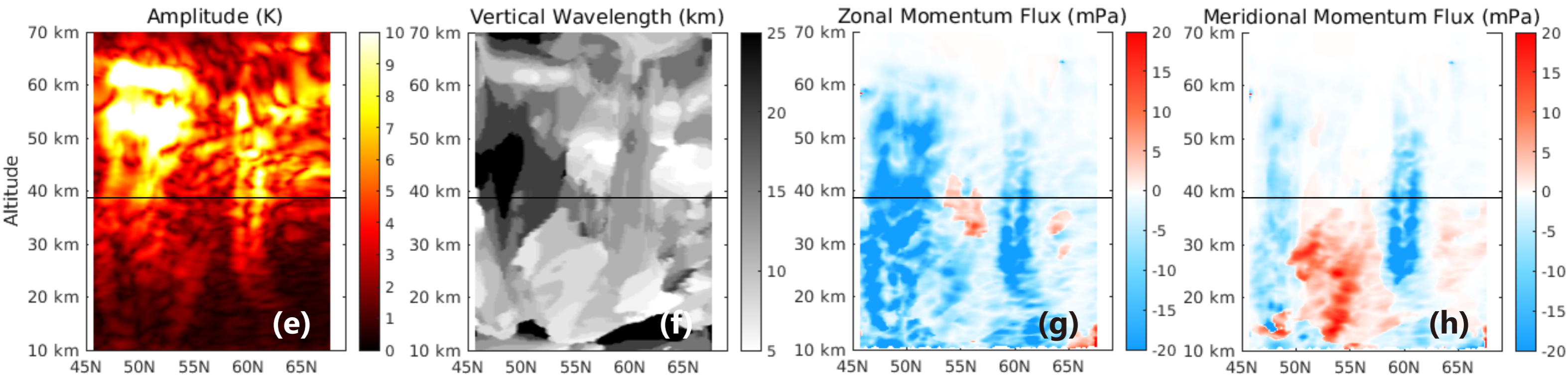
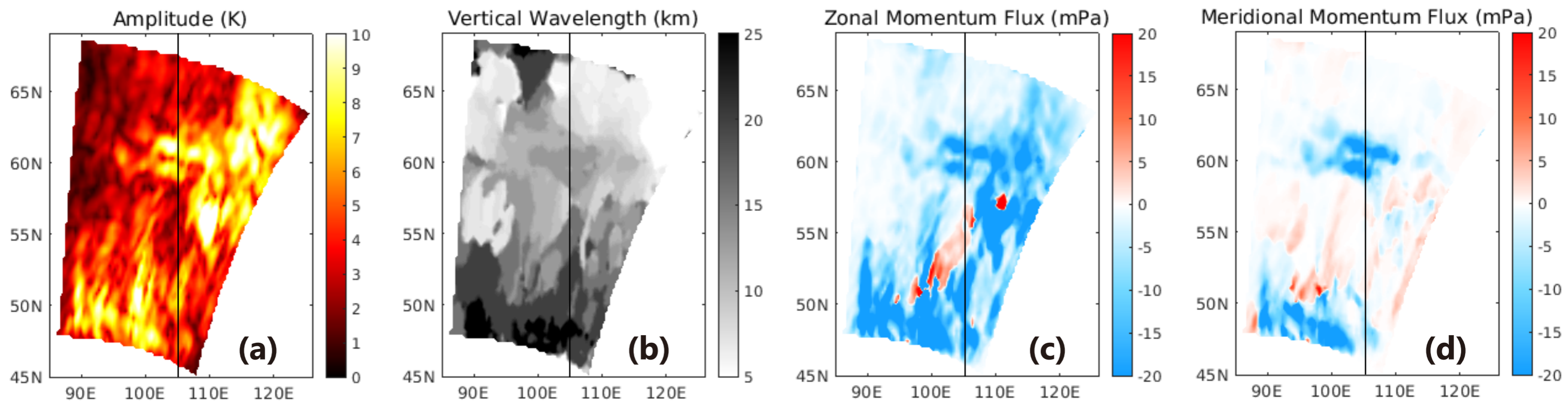


Figure 9.

